

CORTICOMUSCULAR ADAPTATION TO MECHANICAL PERTURBATIONS IN A SEATED  
LOCOMOTOR TASK

by

SEYED YAHYA SHIRAZI

M.Sc. AmirKabir University of Technology (Tehran Polytechnic), 2014  
B.Sc. AmirKabir University of Technology (Tehran Polytechnic), 2011

A dissertation submitted in partial fulfilment of the requirements  
for the degree of Doctor of Philosophy in Mechanical Engineering  
in the Department of Mechanical and Aerospace Engineering  
in the College of Engineering and Computer Science  
at the University of Central Florida  
Orlando, Florida

Spring Term  
2021

Major Professor: Helen J. Huang

© 2021 Seyed Yahya Shirazi

## **ABSTRACT**

Seated locomotor tasks such as cycling or recumbent stepping improve walking performance during rehabilitation. Cortical control during walking is most pronounced when the person is perturbed. But, the electrocortical dynamics during perturbed seated tasks has not been studied in detail. The primary purpose of this research was to quantify cortical and muscular responses to mechanical perturbations during recumbent stepping. We also aimed to quantify possible differences between young and older adults' responses to perturbed stepping. Seventeen young adults and eleven older adults completed four perturbed arms and leg stepping tasks. We perturbed the stepping with brief 200ms increased movement resistance using a controllable servomotor on our recumbent stepper. We asked subjects to step smoothly, use both arms and legs and follow the visual pacing cue set at 60 steps per minute. We used high-density electroencephalography (EEG) with 128 electrodes to record brain activity, 16 electromyography (EMG) sensors to record muscle activity, and stepping kinematics using the servomotor's encoder.

Dedicated to my love, Maryam.

## **ACKNOWLEDGMENTS**

The acknowledgments page is optional. If you choose to use it, it should appear after the Abstract, but before the Table of Contents.

## **TABLE OF CONTENTS**

LIST OF FIGURES . . . . .	x
LIST OF TABLES . . . . .	xviii
CHAPTER 1: INTRODUCTION . . . . .	1
First-level Subheading . . . . .	1
Second-level Subheading . . . . .	1
Third-level Subheading . . . . .	1
Fourth-level Subheading . . . . .	1
Fifth-level Subheading . . . . .	2
CHAPTER 2: More Reliable EEG Electrode Digitizing Methods Can Reduce Source Estimation Uncertainty, But Current Methods Already Accurately Identify Brodmann Areas . . . . .	3
Introduction . . . . .	3
Methods . . . . .	6
Digitizing methods . . . . .	6
Ultrasound . . . . .	8

Structured-light 3D scan . . . . .	8
Infrared 3D scan . . . . .	9
Motion capture probe . . . . .	10
Motion capture . . . . .	10
Transformation to head coordinates . . . . .	10
Digitization reliability and validity . . . . .	11
Digitization reliability . . . . .	11
Digitization validity . . . . .	12
Source estimation uncertainty . . . . .	12
Spatial uncertainty . . . . .	13
Brodmann area accuracy . . . . .	13
Statistical analysis . . . . .	14
Results . . . . .	15
Discussion . . . . .	23
Conclusion . . . . .	31
References . . . . .	32
<b>CHAPTER 3: Influence of Mismarking Fiducial Locations on EEG Source Estimation . .</b>	<b>40</b>

Introduction . . . . .	40
Methods . . . . .	41
Source Estimation and Dipole Fitting . . . . .	42
Dipole Uncertainty Analysis . . . . .	43
Random Fiducial Mismarkings . . . . .	44
Results . . . . .	44
Discussion and Conclusion . . . . .	47
References . . . . .	49
CHAPTER 4: Influence of Mismarking Fiducial Locations on EEG Source Estimation . .	51
Introduction . . . . .	51
Methods . . . . .	53
Experiment procedure and motor errors . . . . .	53
Data collection . . . . .	55
Stride events . . . . .	57
Motor errors . . . . .	57
EEG processing . . . . .	58
Statistical analysis . . . . .	61

Identification of motor responses . . . . .	61
Tests for hypotheses 1 and 2: adaptation of motor and cortical responses . .	61
Tests for hypothesis 3: effect of perturbation timing . . . . .	62
Tests for hypothesis 4, motor cortex lateralization . . . . .	62
Results . . . . .	63
Motor error responses and cortical clusters . . . . .	63
Anterior cingulate theta-band adaptation occurred without motor error adaptation in perturbed strides . . . . .	64
Anterior cingulate theta-band adaptation occurred without motor error adaptation in catch strides . . . . .	65
Perturbations at extension-onset had greater theta-band ERSP in motor cortices than at mid-extension . . . . .	68
Cortical lateralization and specialization . . . . .	68
Discussion . . . . .	69
References . . . . .	74
APPENDIX A: IRB DOCUMENTS . . . . .	81
APPENDIX B: COPYRIGHT PERMISSION LETTERS . . . . .	85

## LIST OF FIGURES

2.2	Visualization of the digitization reliability. Colored and scaled dots show the electrode location within-method variability for all 128 electrodes for the five digitizing methods. Ultrasound had the greatest variability and was the least reliable. The electrodes at the back of the head also tended to have the greatest variability. The motion capture method had the least variability and was the most reliable. The color bar and scale for the radii of the dots illustrate the magnitude of variability. . . . .	16
2.3	<b>A:</b> Reliabilities, quantified as the average variability, were significantly different for the five digitizing methods. The reliability of each digitizing method was significantly different from all other methods (* = Tukey-Kramer p's <0.001 for all pair-wise comparisons). <b>B:</b> Validity, quantified as the average systematic bias showed that the structured-light 3D scan had the largest systematic bias compared to ultrasound and the infrared 3D scan. The motion capture probe method was assumed to be the ground truth and thus has no systematic bias and is not shown. * = Tukey-Kramer p's <0.001. Error bars are the standard deviation. infrared = infrared 3D scan. str.-light = structured-light 3D scan. m.+probe = motion capture probe. mocap = motion capture. . . . .	18
2.4	An example depiction of the synthesized electrode locations with a Gaussian distribution using the same averaged variability and standard deviation as the structured-light 3D scans, and the enclosing ellipsoids of the 500 dipoles for each independent component (IC) and digitizing method. Black dots = centroids of the electrode locations. Light gray dots = first 150 out of 500 synthesized electrode locations. Each color represents a different IC (23 ICs total). A close-up view of the ellipsoid fit for an Anterior Cingulate IC based on the reliability of the ultrasound digitizing method. . . . .	19





3.2	Fiducial mislocations and their corresponding estimated dipoles for <b>A.</b> Left preauricular (LPA), <b>B.</b> Nasion (Nz) and <b>C.</b> Right preauricular (RPA) for three independent components (ICs). Dipoles are located at the anterior cingulate (A.Cing.), the primary somatosensory cortex (Somat.) and at the premotor cortex (Premot.). Lighter colors show positive direction for the fiducial shifts. For each fiducial, resultant dipoles are plotted in sagittal, frontal and top views. . . . .	45
3.3	<b>A.</b> Relationship between the uncertainty volume and fiducial shifts. ICs in Figure 3.2 are drawn in color: anterior cingulate (ant. cingulate), somatosensory cortex (somatosens.) and premotor cortex (premotor). Tetrahedrons represent dipole uncertainty at the anterior cingulate. Pink cubes has the same volume as the tetrahedral volumes, with the same width as the maximum cluster width (D). The green dashed line quadratically models the uncertainty volume as a function of the fiducial shift. <b>B.</b> Maximum cluster width (D) of the dipoles estimated from the equidistant fiducial shifts. The green dashed line relates the maximum cluster width to the fiducial shift. . . . .	46
4.1	<b>Recumbent stepper and perturbations.</b> <b>a.</b> The recumbent stepper is a one-degree-of-freedom arm-leg exercise device. <b>b.</b> Perturbations were applied either at the extension-onset or mid-extension of the targeted leg. Perturbations were increased stepping resistance for 200 milliseconds. <b>c.</b> The experiment included four tasks. Each task had three ordered blocks, pre, perturbed stepping, and post. The perturbed stepping block also included random no-perturbation catch strides. . . . .	54

4.2	<b>Motor error metrics.</b> Subjects were instructed to match the pace and step smoothly. <b>a.</b> Stepping duration (i.e., temporal) error is the difference between stride duration and the two-second pacing cue. <b>b.</b> Stepping position (i.e., spatial) error is the maximum difference between the time-normalized stepping profile and the averaged <i>pre</i> profile. . . . .	56
4.3	<b>EEG post-processing workflow with a novel step-wise algorithmic parameter sweeping noise rejection process.</b> Shaded blocks indicate inputs or outputs. Thick lined blocks highlight the novel step-wise rejection approach. . .	58
4.4	<b>Temporal and spatial errors during perturbed stepping.</b> The <i>perturbed-stepping</i> block include both perturbed strides (green) and one-in-five random catch strides (purple). For <i>perturbed-stepping</i> , the 10 circles are the averages of 10% batches. For <i>pre</i> and <i>post</i> , the 5 circles are the averages of 20% batches. * indicates significant post-hoc LSD tests <b>a.</b> Temporal errors were different between perturbed and catch strides (~50 ms vs ~200 ms) and returned to the <i>pre</i> levels during the <i>post</i> block. <b>b.</b> Spatial error was greater for the perturbed strides than catch strides, and did not return to <i>pre</i> levels during <i>post</i> . . . . .	60
4.5	<b>Locations of the electrocortical clusters.</b> Clusters with sources from > 70% of the subjects are shown. Only one source per subject was selected for each cluster during analysis. "% of all" indicates the percentage of all components in the Brodmann Area. a.u.: arbitrary unit . . . . .	64

4.6	<b>Motor errors and anterior cingulate ERSP</b> <b>a.</b> and <b>d.</b> Adaptation (early vs. late) was not a significant factor for motor errors. # indicates perturbation timing was a significant factor. Error bars indicate confidence interval (CI) <b>b.</b> Perturbations (i.e., the strong solid lines) elicited theta synchronization in anterior cingulate cortex. Right-side perturbations elicited weaker synchronization during the late perturbed strides. <b>c.</b> Average theta-band ERSP waveform shows increased power after the perturbations across the tasks. Late perturbations elicited less theta-band average power only on the right-side tasks. <b>e.</b> Early catches (narrow solid lines) elicited a theta synchronization in the anterior cingulate cortex. <b>f.</b> Average theta-band ERSP waveform shows late right extension-onset catch strides elicited significantly higher spectral power than the early catch. Shaded areas indicate CI. Black bars indicate significant difference between early and late. Colored bars indicate CI does not overlap with zero. . . . .	66
4.7	<b>Motor errors and theta-band ERSP across perturbation timings.</b> <b>a.</b> and <b>b.</b> Task type (mid-extension vs. extension-onset) was a significant factor for motor errors. Error bars indicate confidence interval (CI). <b>c.</b> Extension-onset perturbations had greater anterior cingulate and ipsilateral theta-band ERSP before the perturbation event (the solid vertical line). The theta-band ERSP was not significantly different after the perturbation event, except for the left SMA ipsilateral task. Shaded area indicates confidence interval. Black bars indicate significant difference between perturbation timing. Colored bars indicate CI clearing zero. . . . .	67

- 4.8      **Supplementary motor area (SMA) Lateralization.** **a.** Theta desynchronization in the perturbed recovery step occurred in the right SMA for extension-onset and in the left SMA for the mid-extension (red squares). Only mid-extension perturbations elicited theta desynchronization before the perturbation event (red dashed rectangles). **b.** Mid-extension catch steps elicited theta synchronization before the end of limb extension (red dashed rectangles). Recovery-step theta desynchronization occurred contralaterally during extension-onset, but only occurred in the right SMA during the mid-extension. Red and black indicate specialized and contralateral lateralization respectively. 72

## LIST OF TABLES

## **CHAPTER 1: INTRODUCTION**

Chapter and major headings should be typed in all caps. Note that Chapter titles should be formatted and positioned exactly the same as frontmatter and other major headings. However, chapters with subtitles may be stacked, single-spaced, rather than appear on one line. The Introduction presents an overview of the thesis or dissertation material to be discussed. For sample theses and dissertations, including sample Introductions from your discipline, visit the University Writing Center's Graduate Gateway, located at <http://www.uwc.ucf.edu>. Please be aware that UWC links are for content samples only, not format samples.

### *First-level Subheading*

First-level subheadings are centered, and occur in title case (upper/lower case letters).

### *Second-level Subheading*

Second-level Subheadings are usually centered in title case with no additional formatting.

### *Third-level Subheading*

Third-level subheadings are underlined and left-justified, still in title case.

### *Fourth-level Subheading*

Fourth-level headings look like second-level headings, except that fourth-level headings are justified.

##### Fifth-level Subheading

The maximum number of subheadings you may use is five. The fifth-level subheading is indented and underlined.

## **CHAPTER 2: More Reliable EEG Electrode Digitizing Methods Can Reduce Source Estimation Uncertainty, But Current Methods Already Accurately Identify Brodmann Areas**

### Introduction

Estimating active cortical sources using electroencephalography (EEG) is becoming widely adopted in multiple research areas as a non-invasive and mobile functional brain imaging modality [1–4]. EEG is the recording of the electrical activity on the scalp and is appealing for studying cortical dynamics during movements and decision making due to the high temporal (i.e. millisecond) resolution of electrical signals. One of the challenges of using EEG is that the signal recorded in an EEG electrode is a mixture of electrical activity from multiple sources, which include the cortex, muscles, heart, eye, 60 Hz noise from power lines, and motion artifacts from cable sway and head movements [5, 6]. To meaningfully correlate EEG analyses with brain function, the unwanted source content such as muscle activity, eye blinks, and motion artifacts need to be attenuated or separated from the cortical signal content. A multitude of tools such as independent component analysis, artifact rejection algorithms, and phantom heads have been developed to address the need to separate the source signals to extract the underlying cortical signal [7–11]. Using high-density EEG and improving EEG post-processing techniques have also improved spatial resolution of source estimation to  $\sim 1$  cm in experimental studies [12–17].

Source estimation requires knowing the EEG signals and the locations of the EEG electrodes to estimate the locations of the cortical sources that produced the EEG signals measured on the scalp. An intuitive assumption of source estimation is that precise placement of the EEG electrodes on the scalp is essential for accurate estimation of source locations [18]. Computational studies report

d shifts of 0.5 cm to 1.2 cm in estimated source locations as a result of 0.5 cm (or 5°) error in the electrode digitization [19–23]. For EEG studies conducted inside a magnetic resonance imaging (MRI) device, the electrode locations with respect to the cortex can be captured and processed with less than 0.3 cm position error, which results in near perfect alignment of identified brain areas [15, 24]. However, for studies that do not involve MRI, the electrode locations should be “digitized”, i.e. recorded digitally via a three-dimensional (3D) position recording method [25]. These digitized locations can then be coupled with either a subject-specific or an averaged template of the brain structure obtained from MRI or other imaging techniques to perform EEG source estimation.

Just one decade ago in the mid-2000’s, the main digitizing technologies available were based on ultrasound and electromagnetism, which were expensive, time consuming, and needed trained operators [25, 26]. An ultrasound digitizing system uses differences in ultrasound-wave travel times from emitters on the person’s face and a digitizing wand to an array of receivers to estimate the 3D location of the tip of the digitizing wand with respect to the face emitters. An electromagnetic system tracks the locations of receivers placed on the person’s head and on a wand in an emitted electromagnetic field to estimate the position of the tip of the wand with respect to the head receivers. The environment must be clear of magnetic objects when using an electromagnetic digitizing system, otherwise the electrode locations will be warped [27, 28].

Recent efforts have focused on developing technologies to make digitization more accessible and convenient, mainly by incorporating image-based technologies [29, 30]. For example, using photogrammetry and motion capture methods for digitization can provide accurate electrode locations in a short period of time [31, 32]. Photogrammetry involves using cameras to take a series of color images at different view angles. These images can then be analyzed to identify the locations of specific points in the 3D space [31, 33]. Motion capture typically uses multiple infrared cameras around the capture volume to take simultaneous images to identify the locations of reflective or

emitting markers. If markers are placed directly on the EEG electrodes, a motion capture system could conveniently record the position of all of the electrodes at once [27, 32]. Motion capture could also be used to record the position of the tip of a probe, a rigid body with multiple markers, to digitize 3D locations of the electrodes with respect to the reflective face markers. Several recent commercial digitizing systems use simple motion capture approaches to digitize EEG electrode locations with or without a probe [28, 34–36].

Another option for digitizing EEG electrodes that has also gained much interest recently are 3D scanners. A common approach for 3D scanning is detecting the infrared or visible reflections of projected light patterns with a camera to estimate the shape of an object [37]. The 3D scanned shapes can then be plotted in a software program such as MATLAB, and the locations of specific points on the 3D scanned shape can be determined. Recently, common EEG analysis toolboxes such as EEGLAB [38] and FieldTrip [39] support using 3D scanners to digitize the electrode locations. Studies suggest that 3D scanners can improve digitization accuracy and significantly reduce digitization time [40]. Using other camera-based systems such as time-of-flight scanners and virtual reality headsets were also reported to provide comparable digitization reliabilities as the ultrasound or electromagnetic digitizing methods, while reducing the time spent for digitizing the EEG electrodes [28, 41, 42].

The purposes of this study were 1) to compare the reliability and validity of five digitizing methods and 2) to quantify the relationship between digitization reliability and source estimation uncertainty. We determined source estimation uncertainty using spatial metrics and Brodmann areas. We hypothesized that digitizing methods with less reliability would increase uncertainty in the estimates of the electrocortical source locations. For our analyses, we assumed that all other contributors to source estimation uncertainty such as variability of head-meshes and assumptions of electrical conductivity values were constant.

## Methods

We fitted a mannequin head with a 128-channel EEG cap (ActiveTwo EEG system, BioSemi B.V., Amsterdam, the Netherlands, Figure 2.1A) and used this mannequin head setup to record multiple digitizations of the locations of the EEG electrodes and fiducials, i.e. right preauricular, left preauricular, and nasion [43]. To prevent the cap from moving from digitization to digitization, we taped the cap to the mannequin head (Figure 2.1A). To help ensure that the fiducials were digitized at the same locations for every digitizing method, we marked the fiducials with small 4-mm markers on the mannequin head and with small o-rings on the cap (Figure 2.1A).

### *Digitizing methods*

We compared five methods for digitization: ultrasound, structured-light 3D scanning, infrared 3D scanning, motion capture with a digitizing probe, and motion capture with reflective markers. We calibrated each digitizing device only once and completed collecting data for each digitizing in a single session (see Table S1 in the supplement for the calibration results). We also kept the position of the mannequin head, mannequin head orientation, start and endpoint of digitizing, lighting, and temperature constant to avoid introducing additional sources of error to our data collection and analysis.

For each method, four different members of the laboratory digitized the mannequin head five times (one person performed the digitization twice). All of the operators had prior experience in digitizing and were asked to follow each method's specific guidelines. We imported the digitization data to MATLAB (version 9.4, R2018a, Mathworks, Natick, MA) and performed all analyses in MATLAB.

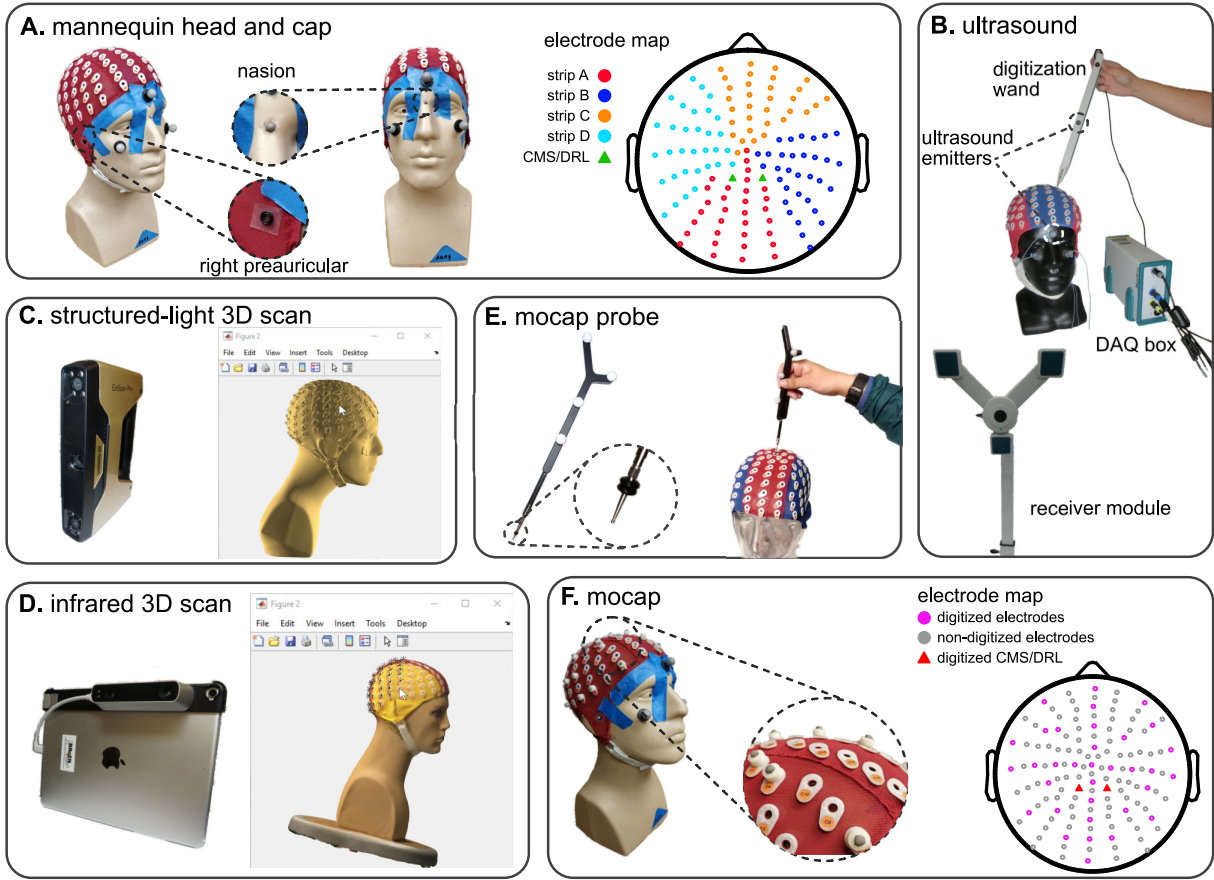


Figure 2.1: The mannequin head used for digitization and the five digitizing methods tested. **A:** The mannequin head fit with the 128-electrode EEG cap used for all of the digitizing recordings. The right and left preauriculars were marked by o-rings and nasion was marked with a reflective marker. The color-coded map of the cap shows the different electrode strips and the order of digitization from A to D. **B:** The ultrasound digitizing system and an operator placing the tip of the wand in the electrode well on the cap. Two of the total five ultrasound emitters on the face and wand, as well as the data acquisition (DAQ) box and the receiver module are also indicated. **C:** The structured-light 3D scanner and an operator manually marking the locations of individual electrodes of the scanned model in MATLAB. **D:** The infrared 3D scanner and an operator manually marking the locations of individual electrodes of the colored 3D scan in MATLAB. **E:** The motion capture digitizing probe with a close-up view of the o-rings placed 7 millimeters away from the tip. The probe has a similar role to the wand in the ultrasound system. **F:** The EEG cap with 35 3D-printed EEG electrode shaped reflective markers, 3 face markers, and 3 fiducial markers used for the motion capture digitization. We placed reflective markers on top of the preauricular o-rings to be able to capture fiducial locations. The electrode map depicts the approximate locations of the digitized electrodes and grounds.

### *Ultrasound*

We used a Zebris positioning system with ElGuide software version 1.6 (Zebris Medical GmbH, Tübingen, Germany, Figure 2.1B) to digitize the electrodes with an ultrasound method. Following the Zebris manual, we placed 3 ultrasound emitters on the face of the mannequin head, placed the receiver module in front of the mannequin head, and used the digitizing wand to record the electrode locations. We calibrated the system using the ElGuide calibration procedure. We marked the fiducials repeatedly until we obtained fiducials with a digitized 3D location of nasion that was  $< 2\text{mm}$  with respect to the midline and with preauriculars that had a difference of  $< 5\text{mm}$  in the anterior/posterior and top/bottom directions. Operators followed the interactive ElGuide template to digitize each electrode location. This process involved fully placing the wand tip into the electrode wells and ensuring that the receivers were able to see all emitters at the time of recording electrode locations, so that the estimated position of the wand tip was stable.

### *Structured-light 3D scan*

We used an Einscan Pro+ (Shining 3D Tech. Co. Ltd., Hangzhou, China, Figure 2.1C) to digitize the electrodes with a structured-light 3D scanner. This scanner estimates the shape of an object from reflections of the projected visible lights. We calibrated the Einscan Pro+ one time with the Einscan's calibration board and followed the software's step-by-step instructions. We used the scanner's hand-held rapid mode with high details and allowed the scanner to track both texture and markers during the scanning process. Each operator scanned the mannequin head until the scan included the cap, fiducials, and the face. We then applied the watertight model option to the scan and exported the model as a PLY file to continue the digitization process in MATLAB.

After acquiring the 3D scan, the 3D head model needed to be imported into a software program,

where the operator manually marked the EEG electrode locations on the 3D scanned head model. We followed the FieldTrip toolbox documentation for digitization using 3D scanners [?] and created a MATLAB script file for importing and digitizing 3D models of the mannequin head. The operator first marked the fiducials on the mannequin head model in MATLAB to build up the head coordinate system. Then, the operator marked the locations of the electrodes on the screen in each section of the cap in alphanumerical order (A, B, C, D, and the fiducials, total: 131 locations, Figure 2.1A). The operators referred to a physical EEG cap for guidance to help mark the locations in the expected order because these scans were not in color and the letter labels of the electrodes were not visible on the 3D model.

### *Infrared 3D scan*

We used the Structure sensor (model ST01, Occipital Inc., San Francisco, CA) integrated with an Apple® iPad (10-inch Pro) to digitize the electrodes with an infrared dot-projection 3D scanner (Figure 2.1D). This scanner shares similar working principles as a structured-light scanner but uses infrared light projection to estimate the shape of objects. We calibrated the sensor in daylight and office light according to the manual. We scanned the head using the high color and mesh resolutions. When the mannequin head was completely in the sensor's field of view, the operator started scanning. The Structure sensor interface gives the operator visual feedback to help the operator obtain a complete high-quality scan. We visually inspected that the scanned model matched the mannequin and then exported the model to the MATLAB environment. We used the FieldTrip toolbox to import and digitize the 3D mannequin head scans following the same procedure described for the structured-light 3D scan digitization.

### *Motion capture probe*

We used a digitizing probe and a 22-camera motion capture system (OptiTrack, Corvallis, OR) to digitize the electrodes. The probe is a solid rigid body with four fixed reflective markers (Figure 2.1E). We placed three reflective makers on the face of the mannequin to account for possible movements of the head during data collection. Each operator digitized the fiducials and each section of the cap (A, B, C, D, Figure 2.1A) in separate takes. We placed double o-rings seven millimeters away from the probe tip to ensure consistent placement of the tip inside the electrode wells (Figure 2.1E). The tracking error of the motion capture system was less than 0.4 millimeters.

### *Motion capture*

We used the motion capture system to record the locations of 35 3D printed reflective markers that resembled a 4-millimeter reflective marker on top of a BioSemi active pin electrode (Figure 2.1F). We did not use actual BioSemi electrodes, which have wires that could prevent the cameras from seeing the markers. We placed 27 EEG electrode shaped markers to approximate the international 10-20 EEG cap layout and placed an additional eight EEG electrode shaped markers randomly on the cap to add asymmetry to improve tracking of the markers. We recorded 2-second takes of the positions of the 35 markers, three markers on the fiducials, and three face markers. Before transforming the locations to the head coordinate system, we identified and canceled movements of the head during data collection using the three face markers.

### *Transformation to head coordinates*

We developed a dedicated pipeline to convert the digitized electrode locations for each digitizing method to a format that could be imported to the common toolboxes for EEG analyses. Because

EEGLAB and FieldTrip can easily read Zebris ElGuide’s output file (an SFP file), we created SFP files for all digitizations.

The head coordinate system in ElGuide defines the X-axis as the vector connecting the left preauricular to the right preauricular and the origin as the projection of the naion to the X-axis. Therefore, the Y-axis is the vector from the origin to the naion, and the Z-axis is the cross product of the X and Y unit vectors, which starts from the origin.

#### *Digitization reliability and validity*

Variations in the digitized electrode locations could originate from random errors and systematic bias. The effects of random errors can be quantified as variability. Reliability is also inversely related to variability. Systematic bias can be quantified as the difference between measured locations and the ground truth locations. Validity is also inversely related to systematic bias.

#### *Digitization reliability*

To assess the effects of random errors, we quantified digitization variability. We averaged the five digitized locations for each electrode to find the centroid. We then calculated the average Euclidean distances of the five digitized points to the centroid for each electrode and averaged those distances for all of the electrodes to quantify within-method variability. We identified and excluded outliers, single measurements that were beyond five standard deviations of the average variability for a digitizing method (1 out of 655 measurements for ultrasound, 4 out of 655 measurements for motion capture probe and 2 out of 190 measurements for motion capture). If there were outliers, we recalculated the average digitization reliability with the updated dataset. Throughout the paper, we use “variability” to refer to “within-method variability.” Because reliability is inversely related to

the variability, the most reliable method has the least variability.

#### *Digitization validity*

To quantify the systematic bias of a digitizing method, we calculated the average Euclidean distance between the centroid for a digitizing method and the ground-truth centroid for the same electrode. We used the electrode centroids from the most reliable digitizing method as the ground-truth [44]. Then, we averaged the Euclidean distances for the 128 electrodes to obtain the magnitude of the systematic bias for each digitizing method. Because validity is inversely related to the systematic bias, the most valid method has the least systematic bias.

#### *Source estimation uncertainty*

To generalize the possible effects of digitization reliability, we synthesized 500 sets of electrode locations with a Gaussian distribution using the variability average and standard deviation calculated for each digitizing method in 2. We excluded the motion capture method from the source estimation uncertainty analyses because we only recorded the locations of 35 EEG electrode shaped reflective markers instead of all 128 EEG electrode locations. We used a single representative 128-channel EEG dataset from a separate study for the source estimation analyses. We applied the Adaptive Mixture Independent Component Analysis (AMICA) to decompose EEG signals into independent components (ICs) [45], which has been reported to represent dipolar activities of different brain and non-brain sources [7].

We used EEGLAB's DIPFIT toolbox version 2.3 to estimate a dipole equivalent for each IC and applied DIPFIT 500 times for each digitizing method. Each DIPFIT iteration used one of the 500 sets of synthesized electrode locations, the Montreal Neurological Institute (MNI) head model [46],

and the ICs from the AMICA. The MNI head model is an averaged structural head model from 305 participants and provides  $1\text{mm} \times 1\text{mm} \times 1\text{mm}$  resolution. To convert the mannequin head to be compatible with the MNI model, we warped the electrode locations to the MNI model using only the fiducials to preserve individual characteristics of the mannequin head. We used the dipoles produced with the electrode location centroids from the digitizing method with the highest reliability and identified the dipoles that described  $> 85\%$  of the IC signal variance. We also excluded any dipole that was estimated to be outside of the brain volume for any of the DIPFIT results ( $500/\text{method} \times$  five methods = 2500 DIPFIT results). In the end, 23 ICs remained.

#### *Spatial uncertainty*

We fitted an enclosing ellipsoid with the minimum volume to each IC's cluster of 500 dipoles [47] and quantified spatial uncertainty in terms of the volume and width of the ellipsoid. A larger ellipsoid volume indicated that a single dipole could reside within a larger volume, and thus, had greater volumetric uncertainty. A larger ellipsoid width indicated that a single dipole could have a larger shift in location. We calculated the ellipsoid's width as the maximum distance that the IC's dipoles could have from one another. We averaged the volumes and widths of all 23 ICs to quantify the spatial uncertainty for each digitizing method.

#### *Brodmann area accuracy*

To identify Brodmann areas, we used a modified version of the `eeg_tal_lookup` function from EEGLAB's Measure Projection Toolbox (MPT). This function looks for the anatomic structures and Brodmann areas in a 10-mm vicinity of each dipole and assigns the dipole to the Brodmann area with the highest posterior probability [48, 49]. We identified the "ground-truth" Brodmann areas from the dipoles estimated using the centroid electrode locations of the most reliable digitizing

method. Then, we calculated Brodmann area accuracy as the percentage of the other 500 Brodmann area assignments that matched the “ground-truth” Brodmann area.

We also analyzed Brodmann area accuracy using a template of electrode locations based on the MNI head model [50]. Because the BioSemi 128-electrode cap is not based on the 10-10 electrode map, instead of using the 10-10 electrode locations, we warped the BioSemi electrode locations to reside on the outer surface of the MNI head model. We then compared the Brodmann area identified from the template to the “ground-truth” Brodmann area. Since there is only one template for the Biosemi 128-electrode location on the MNI head model and the locations are fixed, we could not calculate a percentage of assignments; thus, the template’s Brodmann area for each IC was either a hit or miss. However, we did calculate and compare the distance between the template’s dipole to the “ground truth” dipole. We also compared the distance between each digitizing method’s dipoles to the “ground truth” dipole. These distances indicated whether the dipoles estimated using each digitization method were near the “ground truth” dipole.

#### *Statistical analysis*

We used a one-way repeated measures analysis of variance (rANOVA) to compare the reliability and validity of the digitizing methods, the spatial uncertainty of the estimated dipoles, and the Brodmann area accuracy. For significant rANOVA’s, we performed Tukey-Kramer’s post-hoc analysis to determine which comparisons were significant. We also performed a one-sided Student t-test to identify if the Brodmann area accuracy of each digitizing method was different from the template. The level of significance for all statistics was  $\alpha = 0.05$ . For rANOVA, we reported degrees of freedom (DF), Fisher’s F-test result and the probability value (p-value). We used p-values to report post-hoc and Student t-test results.

Additionally, we fit a polynomial, using a step-wise linear model (MATLAB `stepwiselm` function),

to describe spatial uncertainty as a function of digitization variability. We forced the y-intercept of the first-order polynomials and the y-intercept and y'-intercept of the higher-order polynomials to be zero. We set the y-intercepts to be zero for two reasons: 1) when we used the exact same electrode locations and performed DIPFIT 100 times, the maximum distance between source locations was on the order of  $10^{-4}$  cm, and 2) the fit should not model the uncertainty values  $< 0$  for positive digitization variability values. The step-wise linear model started with a zero order model and only added a higher-order polynomial term when necessary. The criterion for adding a higher-order polynomial term to the model was a statistically significant decrease of the sum of the squared error between the data points and the predicted values.

## Results

The variability results for the five digitizing methods were visibly different, and electrodes located at the back of the head tended to have greater variability (Figure 2.2). The variability for the ultrasound method was generally largest compared to the other methods and could be as large as  $\sim 1.5$  cm for electrodes at the back of the head. The variability for all electrodes digitized with the motion capture method was small, being no greater than 0.001 cm.

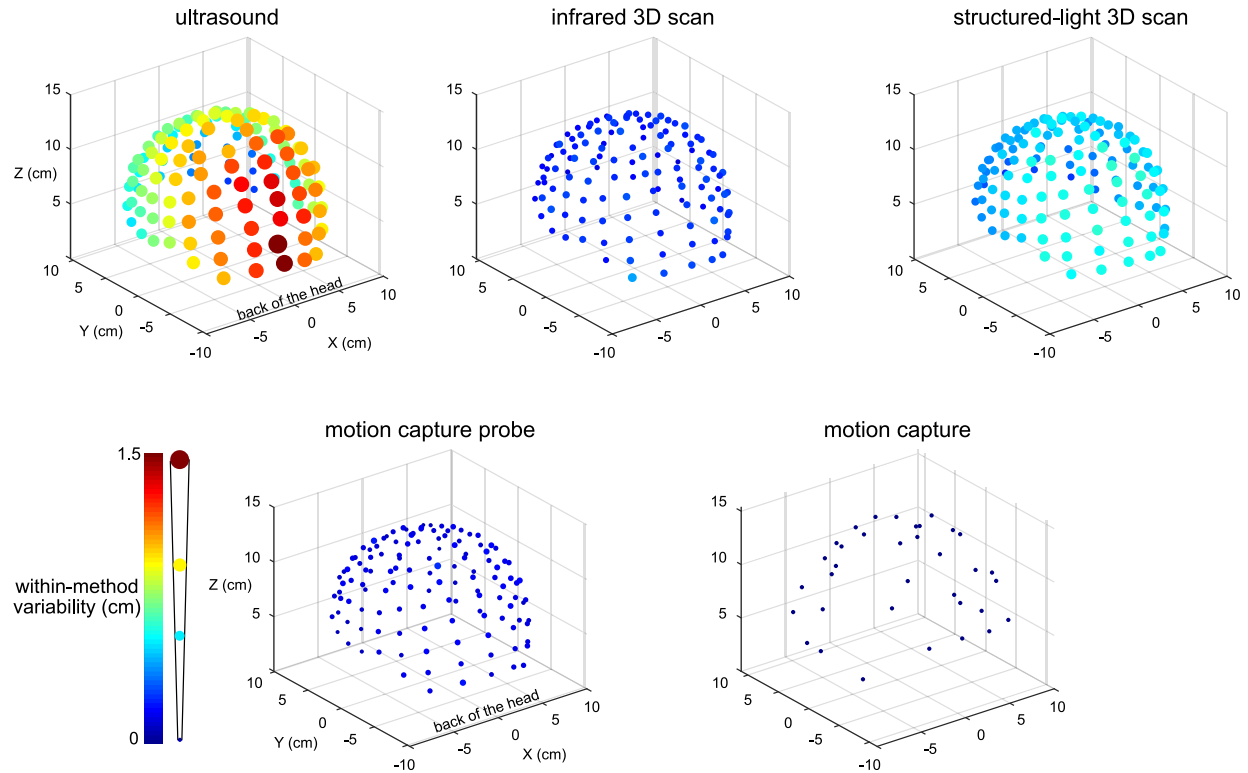


Figure 2.2: Visualization of the digitization reliability. Colored and scaled dots show the electrode location within-method variability for all 128 electrodes for the five digitizing methods. Ultrasound had the greatest variability and was the least reliable. The electrodes at the back of the head also tended to have the greatest variability. The motion capture method had the least variability and was the most reliable. The color bar and scale for the radii of the dots illustrate the magnitude of variability.

There was a range of reliabilities among the digitizing methods (Figure 2.3A). The motion capture digitizing method had the smallest variability of  $0.001 \pm 0.0003$  cm (mean  $\pm$  standard deviation) and hence, the greatest digitization reliability. The motion capture probe was the next most reliable method with an average variability of  $0.147 \pm 0.03$  cm, followed by the infrared 3D scan ( $0.24 \pm 0.05$  cm), the structured-light scan ( $0.50 \pm 0.09$  cm), and the ultrasound digitization ( $0.86 \pm 0.3$  cm). The variability for the digitizing methods were significantly different (rANOVA DF=4, F=1121, p<0.001), and the variability for each digitizing method was significantly different from

all other digitizing methods (post-hoc Tukey-Kramer, p's <0.001).

The systematic biases, thus validities, of the digitizing methods were significantly different (rA-NOVA DF=2, F=143.1, p<0.01, Figure 2.3B). The digitization validity of the structured-light 3D scan was the worst of the digitizing methods with a systematic bias of  $0.63 \pm 0.18$  cm that was significantly larger than the other digitizing methods (post-hoc Tukey-Kramer, p's <0.001). The digitization validity of the ultrasound and the infrared 3D scans were similar, with systematic biases of  $0.43 \pm 0.18$  cm and  $0.41 \pm 0.13$  cm, respectively.

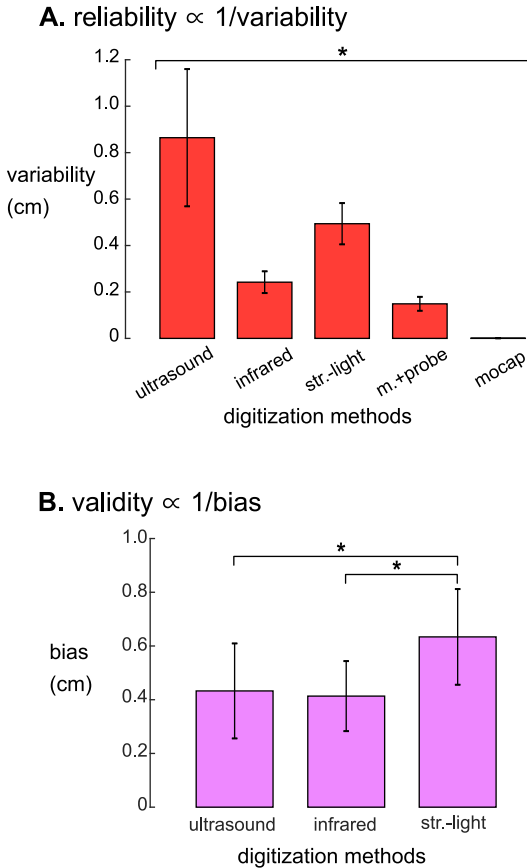


Figure 2.3: **A:** Reliabilities, quantified as the average variability, were significantly different for the five digitizing methods. The reliability of each digitizing method was significantly different from all other methods (\* = Tukey-Kramer p's <0.001 for all pair-wise comparisons). **B:** Validity, quantified as the average systematic bias showed that the structured-light 3D scan had the largest systematic bias compared to ultrasound and the infrared 3D scan. The motion capture probe method was assumed to be the ground truth and thus has no systematic bias and is not shown. \* = Tukey-Kramer p's <0.001. Error bars are the standard deviation. infrared = infrared 3D scan. str.-light = structured-light 3D scan. m.+probe = motion capture probe. mocap = motion capture.

Within a given digitizing method, dipoles generally showed similar spatial uncertainty while different digitizing methods generally showed differences in spatial uncertainty (Figure 2.4). Ellipsoid sizes for the motion capture probe, infrared 3D scan, structured-light 3D scan, and ultrasound digitization increased in order from the smallest to the largest, respectively. The enclosing ellipsoids of adjacent

ICs also overlapped when the ellipsoid size was large, on the order of  $1 \text{ cm}^3$ , such as for the ultrasound method.

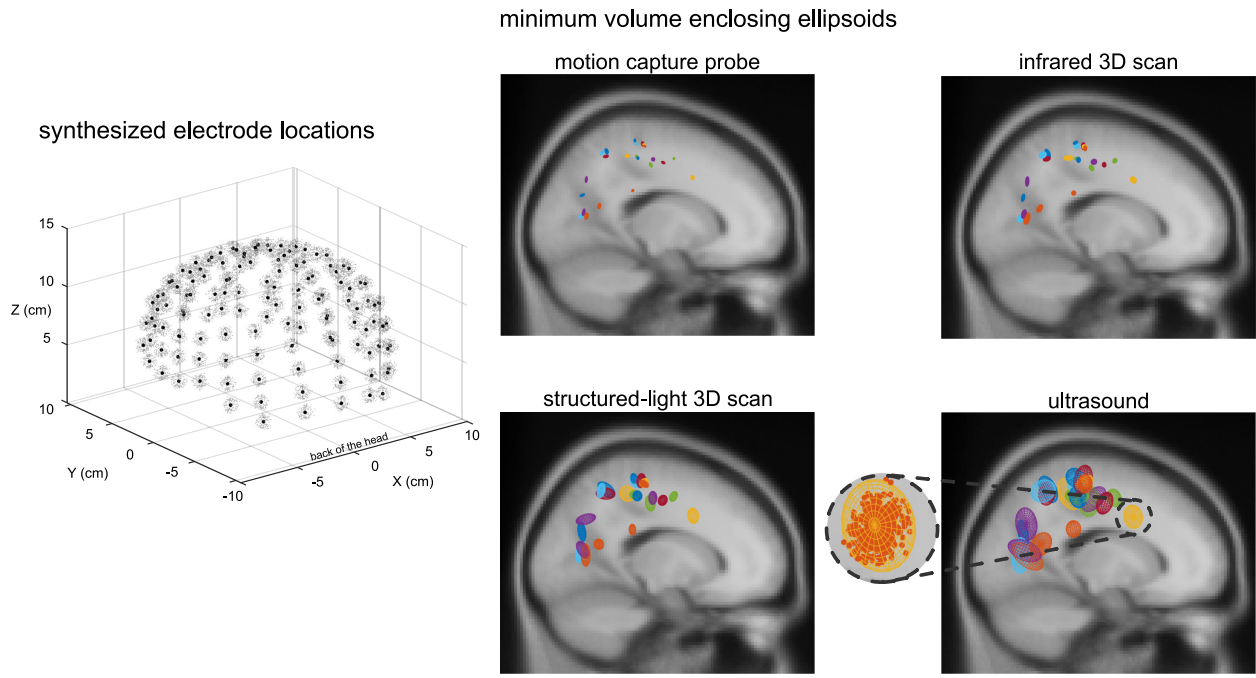


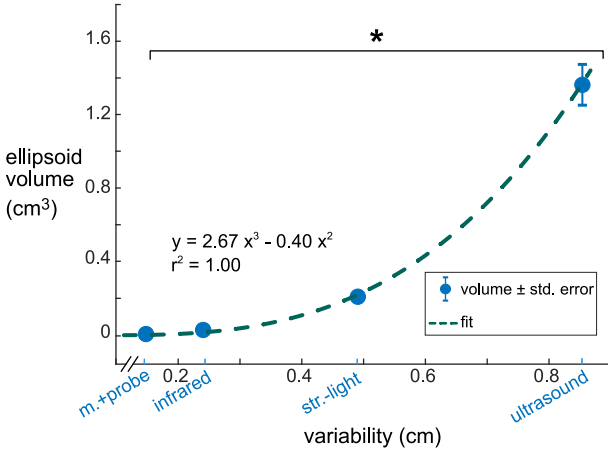
Figure 2.4: An example depiction of the synthesized electrode locations with a Gaussian distribution using the same averaged variability and standard deviation as the structured-light 3D scans, and the enclosing ellipsoids of the 500 dipoles for each independent component (IC) and digitizing method. Black dots = centroids of the electrode locations. Light gray dots = first 150 out of 500 synthesized electrode locations. Each color represents a different IC (23 ICs total). A close-up view of the ellipsoid fit for an Anterior Cingulate IC based on the reliability of the ultrasound digitizing method.

Ellipsoid volumes increased significantly with increasing digitization variability among the digitizing methods and had a cubic relationship ( $r^2 = 1.00$ , Figure 2.5A). The motion capture probe and infrared 3D scan had the smallest uncertainty volumes (mean  $\pm$  standard error)  $0.007 \pm 0.0007 \text{ cm}^3$  &  $0.029 \pm 0.0027 \text{ cm}^3$ , respectively, whereas ultrasound had the largest uncertainty volume ( $1.37 \pm 0.13 \text{ cm}^3$ ). Structured-light 3D scan had an average uncertainty volume of  $0.21 \pm 0.014 \text{ cm}^3$ . The volumes of the enclosing ellipsoids showed a significant between-group difference (rANOVA,

$DF=3$ ,  $F=114.4$ ,  $p<0.001$ ), and all uncertainty volume combinations of paired digitizing methods were significantly different (Tukey-Kramer post-hoc,  $p's<0.001$ ).

Ellipsoid widths also increased significantly with increasing digitization variability among the digitizing methods but had a linear relationship where the ellipsoid width was twice the size of the digitization variability ( $r^2 = 1.00$ , Figure 2.5B). The average ellipsoid width was the smallest for the motion capture probe, (mean  $\pm$  standard error)  $0.34 \pm 0.018$  cm. The average ellipsoid widths for the two 3D scans were  $0.53 \pm 0.028$  cm for the infrared 3D scan and  $1.09 \pm 0.051$  cm for the structured-light 3D scan. The largest average ellipsoid width was for the ultrasound digitization,  $1.90 \pm 0.081$  cm. The rANOVA for the widths of the enclosing ellipsoids showed a significant between-group difference ( $DF=3$ ,  $F=434.8$ ,  $p<0.001$ ) and all combinations of paired digitizing methods had significantly different uncertainty widths (Tukey-Kramer post-hoc  $p's<0.001$ ).

### A. spatial uncertainty: ellipsoid volume



### B. spatial uncertainty: ellipsoid width

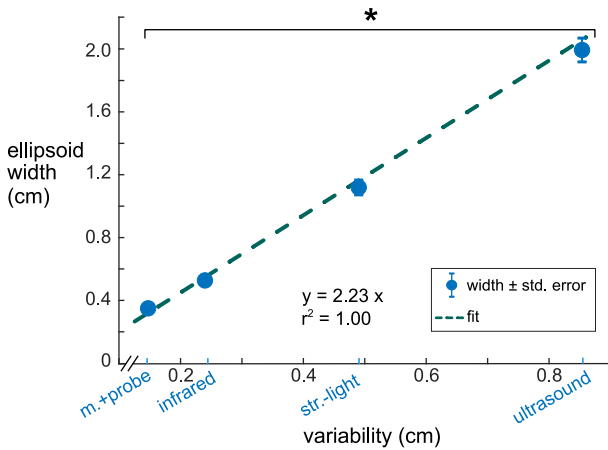


Figure 2.5: The relationships between digitization variability and dipole spatial uncertainty. **A:** Digitization variability and ellipsoid volume had a cubic relationship with an  $r^2$  of 1.00. **B:** Digitization variability and ellipsoid width had a linear relationship with an  $r^2$  of 1.00. Error bars are the standard error. \* = Tukey-Kramer p's <0.001 for all pair-wise comparisons. m.+probe = motion capture probe. infrared = infrared 3D scan. str.-light = structured-light 3D scan.

The Brodmann area accuracy among the digitizing methods could be extremely consistent within some ICs and could also be drastically different for other ICs (Figure 2.6 and in Supplement Figure S1). In general, the digitizing method with the highest reliability also had the highest Brodmann

area accuracy within a given IC. For some ICs, all digitizing methods had  $> 98\%$  Brodmann area accuracy. For other ICs, the Brodmann area accuracy decreased as reliability decreased. The most drastic example for this dataset was BA18 in Figure 2.6, where the Brodmann area accuracy was 86% with the motion capture probe method but dropped to 26% with the ultrasound method.

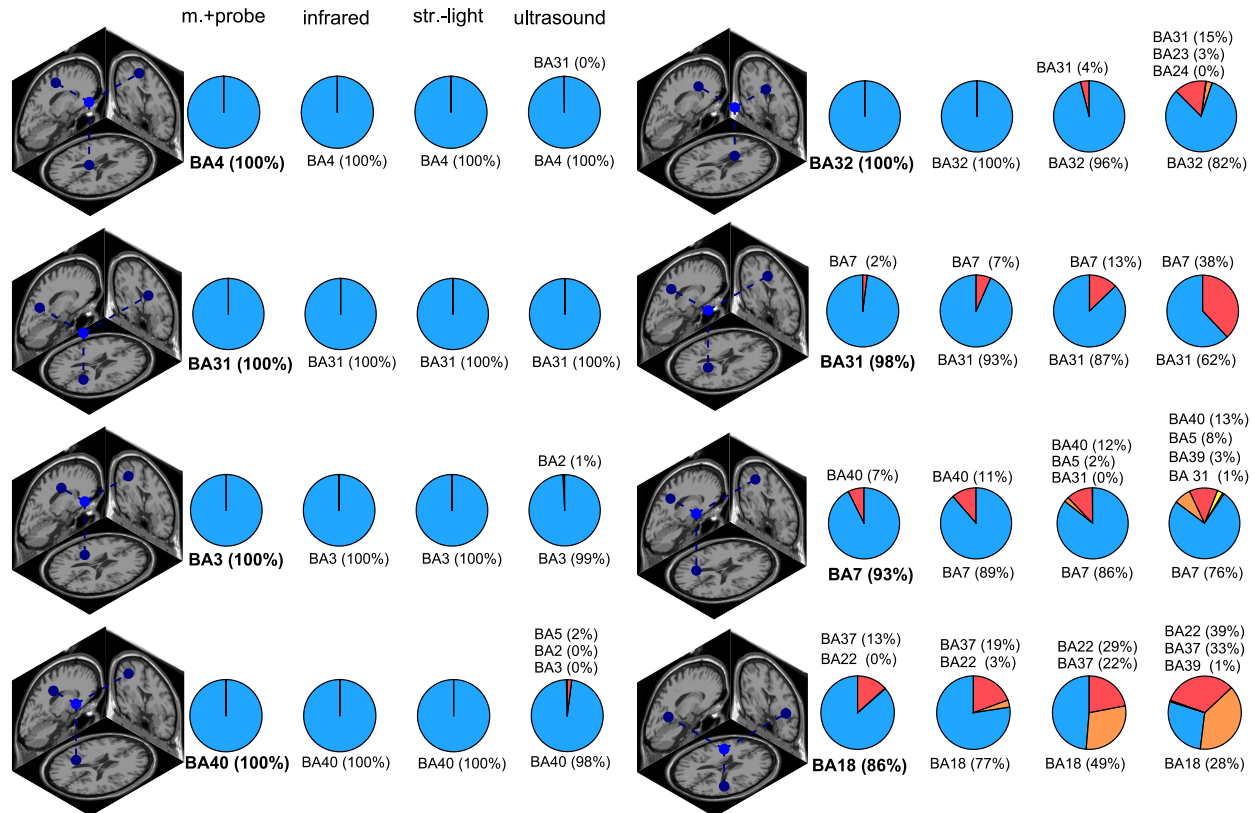


Figure 2.6: Brodmann area (BA) accuracy for a subset of ICs. The dipole depicts the “ground truth” dipole produced from the most reliable digitizing method, the motion capture probe method. The pie charts show the distribution of the Brodmann area assignments compared to the “ground truth” Brodmann area (shown in bold). ICs in the left column had consistent Brodmann area assignments regardless of digitizing method while the ICs in the right column had more varied Brodmann area assignments for the different digitizing methods. In general, less reliable digitizing methods led to less consistent Brodmann area assignments.

The Brodmann area accuracy for the digitizing methods and the template were significantly different

(Figure 2.7). The motion capture probe had the highest Brodmann area accuracy,  $93\% \pm 16$  (mean  $\pm$  standard deviation). The remaining digitizing methods in order of decreasing Brodmann area accuracy were the infrared 3D scan ( $91\% \pm 19\%$ ), the structured light 3D scan ( $87\% \pm 23\%$ ), and the ultrasound digitization ( $79\% \pm 25\%$ ). The rANOVA for the Brodmann area accuracy showed a significant between-group difference ( $DF=4$ ,  $F=306.4$ ,  $p<0.001$ ). Post-hoc Tukey-Kramer analysis showed significant pair-wise difference between all groups except the motion capture probe and infrared 3D scan. Using the MNI electrode template decreased the Brodmann area accuracy to 53% and was significantly different compared to any of the digitizing methods ( $p's<0.001$ ). The average distance of the dipoles of each digitizing method to the “ground-truth” dipole was less than 0.4 cm while the average distance of the template dipoles to the “ground-truth” dipole was  $\sim 1.4$  cm.

## Discussion

We found that there was a range of reliability and validity values among the digitizing methods. We also observed that less reliable digitizing methods translated to greater uncertainty in source estimation and poorer Brodmann area accuracy, assuming all other contributors to source estimation uncertainty were constant. Of the five digitizing methods (ultrasound, structured-light 3D scan, infrared 3D scan, motion capture probe, and motion capture), the most reliable digitizing method was the motion capture while ultrasound was the least reliable. The structured-light digitizing method had the greatest systematic bias and was thus the least valid method. We had hypothesized that less reliable digitizing methods would lead to greater source estimation uncertainty. In support of our hypothesis, digitizing methods with decreased reliability resulted in increased spatial uncertainty of the dipole locations and decreased Brodmann area accuracy. Surprisingly, any digitizing method led to an average Brodmann area accuracy of  $>80\%$ . Using a template of electrode locations decreased Brodmann area accuracy to 53%. Overall, these results indicate that electrode digitization is crucial

for accurate Brodmann area identification using source estimation and that more reliable digitizing methods are beneficial if the functional resolution for interpreting source estimation is more specific than Brodmann areas.

To help summarize the advantages of the different digitization systems, we created a table comparing the digitization reliability, dipole uncertainty, speed, affordability, and ease-of-use score, which are different factors that could influence which digitization a laboratory might choose to use (Table 2.1). We estimated the digitizing speed as how much time each digitization required. The fastest digitizing method that required manual electrode marking was the motion capture probe method, which took 5 minutes to mark each electrode and 5 minutes to calibrate the system. The least expensive system was the infrared 3D scanner, which is likely to become even less expensive as cameras on smartphones become more advanced and could soon be used to obtain an accurate 3D scan for digitizing EEG electrodes. We also surveyed the operators to score each digitization on a scale of 1-5, with 1 being easy to use. While performing the actual 3D scan was perceived as being easy, marking the electrodes in MATLAB was not an easy task. The operators indicated that the motion capture was the easiest and that ultrasound was the most difficult method to use. To create a final ranking, we averaged the rankings for each factor (digitization reliability, dipole uncertainty, speed, affordability, and ease-of-use) to obtain a method score. Based on the method score, the best digitizing method was the motion capture. The next best method was tied between the motion capture probe and infrared 3D scan. The fourth best digitizing method was the structured-light 3D scan, and the worst digitizing method was the ultrasound method, which ranked poorly for all factors.

Our results suggest that the motion capture method currently provides the most reliable electrode digitization. The average variability of the motion capture digitization was less than the mean calibration error reported by the motion capture system (0.001 versus <0.04 cm respectively). This difference might be because of the different natures of the two variabilities. The digitization

variability is defined for a seated subject (or mannequin) and multiple sub-second snapshots of the static electrodes placed on the cap. However, the mean calibration error is defined for a set of moving markers in a much larger volume across several minutes of a calibration period. Using the same position for mannequin placement and lack of head movement may have also contributed to the small digitization variability using motion capture. In a previous study, Reis and Lochmann developed an active-electrode motion capture approach for an EEG system with 30 electrodes and reported small deviation of the digitized locations from the ground truth locations [32]. In addition to having sub-millimeter variability, the motion capture method only required 1-2 seconds to digitize, assuming that the markers were already placed on the EEG electrodes. However, tracking 64+ markers on an EEG cap may be challenging for most motion capture systems. Determining the maximum number of EEG electrodes that could be digitized using a motion capture approach could be beneficial and pursued in future work. Laboratories that already have a motion capture system and do not need to digitize more than 64 EEG electrodes could conveniently use the motion capture method, which would provide a cost-effective, fast, and easy digitizing process. For laboratories that need to digitize 64+ electrodes and have a motion capture system already, the motion capture probe digitizing method would be the recommended option.

Our results support recent efforts to use 3D scanners as a reliable and cost-effective method to digitize EEG electrodes [40, 51, 52]. Both the structured-light and infrared 3D scanning methods were more reliable than digitizing with the ultrasound method. Furthermore, our reliability results for the two 3D scanners align well with a recent study that showed that an infrared 3D scan could automatically digitize electrode locations on three different EEG caps and achieve good reliability after additional post-processing [40]. Of the two 3D scanners we tested, the less expensive infrared 3D scanner was more reliable, had higher validity, and resulted in less dipole uncertainty, compared to the structured-light 3D scanner. Even though the structured-light 3D scanner provides more details from the mannequin head and cap, those details did not seem to be important for improving

digitization reliability or validity. Additionally, the highly detailed structured-light 3D scans created large files and resulted in sluggish refresh rates that made using FieldTrip toolbox to rotate and manipulate the 3D scans difficult. The infrared 3D scan, unlike the structured-light 3D scan, was in color, which was helpful for the operators to identify the EEG electrodes more easily on the computer screen. In the future, artificial intelligence approaches may be able to fully automate the digitizing process and use the additional topographic details from high resolution 3D scans. A continuous image-based digitizing method such as using a regular video recorded using a typical smartphone could also potentially be developed to digitize EEG electrode locations.

Compared to simulation studies, our experimental results demonstrated that source estimation uncertainty increased steeply with increasing EEG electrode variability. We showed that a digitizing method with an average variability of 1 cm could lead to a shift of a single dipole by more than 2 cm, which is  $> 20\%$  of the head radius. There is just one simulation study that we know of that also showed a 2-fold increase in source uncertainty for every unit of digitization variability [23]. In that study, digitization variabilities were created using systematic rotations applied to every electrode location. The majority of the simulation studies however, suggest that source uncertainty could only be as large as the digitization variability [20–22, 53]. In one of the mathematical studies, the theoretical lower bound of source estimation uncertainty was 0.1cm for 0.5cm shifts in EEG electrode location [22], which is 10x smaller than our experimental results. While simulation studies can be insightful, results should also be cross-validated with a conventional source estimation method (e.g. DIPFIT, LORETA or minimum norm) to determine whether simulation results are indicative of real-world source estimation uncertainty.

Because researchers often use Brodmann areas to describe the function of a source, we translated our results to be in terms of Brodmann area accuracy, which led to a few surprising revelations. The main revelation was that despite the range of digitization reliabilities, any of the digitizing methods we tested produced an average Brodmann area accuracy  $> 80\%$ . As long as sources are

only discussed according to Brodmann areas or larger cortical spatial regions, any current digitizing method can be used. The second revelation was that using the template electrode locations, instead of digitizing the electrodes, significantly decreased Brodmann area accuracy from  $> 80\%$  to  $\sim 50\%$ , which may be due to a  $\sim 1.5\text{cm}$  shift in dipoles locations (Figure 2.7). This shift may occur because the template removes information related to individual's head shape. The third revelation was that for several sources, the same Brodmann area was almost always identified, regardless of the digitizing method used (left column in Figure 2.6). For other sources, less reliable digitizing methods led to more potential Brodmann area assignments (right column in Figure 2.6), but those different Brodmann areas may be functionally similar. Most likely, the proximity of a source to the boundary of a Brodmann area as well as the size of the Brodmann area contribute to Brodmann area accuracy. Ultimately, the accuracy of source estimation will depend on the target volumes of cortical regions of interest.

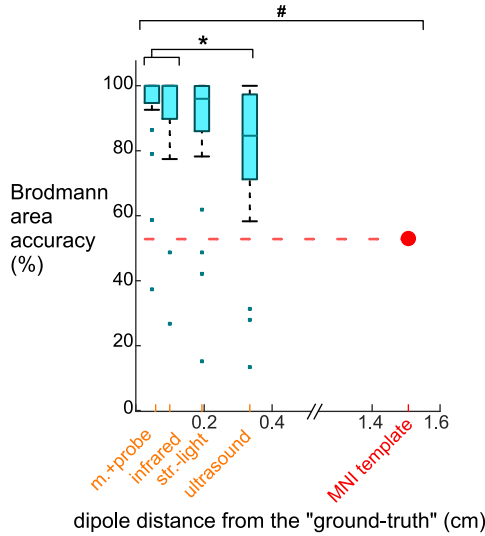


Figure 2.7: Brodmann area accuracy plotted versus the average dipole distance from the “ground truth” dipole when using different digitizing methods and the MNI template. Because larger distances between the dipoles and the “ground truth” likely would decrease Brodmann area accuracy, we plotted the methods on the x-axis at the method’s averaged dipole distance from the “ground truth” dipole. The box-whisker plot contains the Brodmann area accuracy averages for the 23 ICs. The Brodmann area accuracy average for an IC was the average of the percentage of the 500 iterations when the Brodmann area identified matched the “ground truth” Brodmann area for that IC. For the template, 53% of the Brodmann areas assigned for the 23 ICs using the template matched the “ground truth” Brodmann area. The Brodmann area accuracy was significantly different among the digitizing methods, except between the motion capture probe and infrared 3D scan (\* Tukey-Kramer p’s <0.001). The template’s Brodmann area accuracy was significantly different than all digitizing methods (# Student’s t-test p’s <0.001). m.+probe = motion capture probe. infrared = infrared 3D scan. str.-light = structured-light 3D scan.

This study does not account for all of the possible sources of errors contributing to digitizing EEG electrodes or source estimation. We placed markers on the fiducials to control for the digitization error of the fiducials, but in practice, marking the fiducials while the subject wears the cap can be challenging. Mismarking a fiducial can significantly shift every dipole location by 2 times the distance of the fiducial mismarking [54]. We also used a mannequin to control for the head movements and relative cap movements to the head. In reality, participants may move their head

and the cap may slightly change position during digitization or data collection that would affect the location of the EEG electrodes with respect to the head. Further, we only calibrated our digitizing devices once for multiple data collections. Nevertheless, in a real laboratory setup, device calibration might be required before each instance of data collection. We, however, included digitization by multiple experienced operators to acknowledge that in a research laboratory different members might complete the digitization for different participants. Overall, our results suggest that as long as all sources of digitization error do not create variability  $> 1$  cm, Brodmann area accuracy would be  $> 80\%$ . Using the same electrical head model and source localization approach helped us to only quantify the effects of digitization variability on source estimation uncertainty. In reality, the EEG signal noise, number and distribution of EEG electrodes, electrical properties of the head model, head model shape and mesh accuracy, and solving approach are among the other potential contributors to source estimation uncertainty [23, 44, 55–58].

Limitations of this study were that we tested a subset of all digitizing methods, used a mannequin head, and not an actual human head for the digitization, and did not perform source estimation using other common algorithms. Even though we did not test many of the marketed digitizing systems, we replicated and tested the fundamental methods used by most of the marketed digitizing systems. One widely used EEG electrode digitizing method we did not test is an electromagnetic digitizing method (e.g. Polhemus Patriot or Fastrack system). Another study using similar digitization reliability analyses reported an average variability of 0.76cm for an electromagnetic digitization system [31], which is slightly better than the ultrasound digitizing method, with a variability of  $0.86 \pm 0.3$ cm. Collecting digitization data from an actual participant might have helped in having a better distribution of the sources inside the brain volume, but we decided to use a mannequin to better control for head movements, relative cap movements and other environmental factors. Here, we used the EEG data only to provide a platform to understand the relationship between the digitization variability and source uncertainty, and locations of the sources do not have any

neurological implications. Last, we did not use other different source estimation algorithms such as LORETA or beam-forming. Studies indicate that commonly used source estimation algorithms generally identify the similar source locations [56, 57, 59], which suggests that the choice of the source estimation algorithm used would probably not significantly alter our results.

Table 2.1: Rankings for each digitizing method based on factors related to performance, cost, and convenience. # is the rank of each method among all five methods and for the specified factor. The digitization reliability values and dipole uncertainty scalar width values were taken from our results. Speed was the approximate time a digitizing method required to obtain the file of electrode locations. The ease-of-use score was the average score operators provided in a survey with a score of 5 being the most difficult and 1 being the easiest method to do. The method score is the average rank of all factors for a given method and was defined as  $score = \sum \# / N$ . Dipole uncertainty was not available for motion capture digitization. Mocap = motion capture. Str.-Light 3D = structured-light 3D scan. \* The probe price is for the OptiTrack digitizing probe. \*\* motion capture cost was for an eight-camera system (Optitrack Flex13, \$8000) and the Optitrack Motive software (\$3000).

method	digitization reliability		dipole uncertainty		speed		affordability		ease-of-use (1 is easiest)	method score (lower is better)
	mean ± SD (cm)	#	mean ± SD (cm)	#	time (min)	#	cost (USD)	#		
ultrasound	0.86 ± 0.30	5	1.90 ± 0.39	4	30	5	15k	5	4.2	4.6
infrared 3D scan	0.24 ± 0.05	3	0.53 ± 0.136	2	20 (10 for scan + 10 for marking in software)	3	1k	1	2.5	2.3
str.-light 3D scan	0.50 ± 0.09	4	1.09 ± 0.24	3	25 (10 for scan + 15 for marking in software)	4	5k	2	3.4	3.3
mocap probe	0.15 ± 0.03	2	0.34 ± 0.08	1	10 (5 for digitizing + 5 for calibration)	2	1k* (probe) 12k** (+mocap)	4	2	2.2
mocap	0.001 ± 0.0003	1	N/A	-	5.1 (0.1 for digitizing + 5 for calibration)	1	11k**	3	1	1.5

Future efforts to improve source estimation, so that sources can be interpreted in terms of cortical spatial regions smaller than Brodmann areas, will involve more than just developing more reliable, convenient, and cost-effective digitizing methods to help reduce source estimation uncertainty. Even if a perfect digitizing method could be developed, there would still be uncertainty in source

estimation as result of other factors such as improper head-model meshes and inaccurate electrical conductivity values [55, 58], which were assumed to have a constant contribution to the source estimation uncertainty in our analyses. Obtaining and using as much subject specific information, such as subject-specific MRI scans in addition to digitizing EEG electrode locations, should improve source estimation. EEGLAB’s Neuroelectromagnetic Forward Head Modeling Toolbox (NFT) could be used to warp the MNI head model to the digitized electrode locations to retain the individual’s head shape but is computationally expensive [60]. Using subject-specific MRIs instead of the MNI head model is also limited to groups with access to an MRI at an affordable cost per scan.

## Conclusion

In summary, there was a range of digitization reliabilities among the five digitizing methods tested (ultrasound, structured-light 3D scanning, infrared 3D scanning, motion capture with a digitizing probe, and motion capture with reflective markers), and less reliable digitization resulted in greater spatial uncertainty in source estimation and poorer Brodmann area accuracy. We found that the motion capture digitizing method was the most reliable while the ultrasound method was the least reliable. Interestingly, Brodmann area accuracy for a source only dropped from  $\sim 90\%$  to  $\sim 80\%$ , when using the most and least reliable digitizing methods, respectively. If source locations will be discussed in terms of Brodmann areas, any of the digitizing methods tested could provide accurate Brodmann area identification. Using a template of EEG electrode locations, however, decreased the Brodmann area accuracy to  $\sim 50\%$ , suggesting that digitizing EEG electrode locations for source estimation results in more accurate Brodmann area identifications. Even though digitizing EEG electrodes is just one of the factors that affects source estimation, developing more reliable and accessible digitizing methods can help reduce source estimation uncertainty and may allow sources to be interpreted in terms of cortical regions more specific than Brodmann areas in the future.

## References

- [1] A. C. Tsolaki, V. Kosmidou, I. Y. Kompatsiaris, C. Papadaniil, L. Hadjileontiadis, A. Adam, and M. Tsolaki, “Brain source localization of MMN and P300 ERPs in mild cognitive impairment and alzheimer’s disease: a high-density EEG approach,” *Neurobiol. Aging*, vol. 55, pp. 190–201, July 2017.
- [2] C. Bradley, N. Joyce, and L. Garcia-Larrea, “Adaptation in human somatosensory cortex as a model of sensory memory construction: a study using high-density EEG,” *Brain Struct. Funct.*, vol. 221, pp. 421–431, Jan. 2016.
- [3] E. C. Landsness, M. R. Goldstein, M. J. Peterson, G. Tononi, and R. M. Benca, “Antidepressant effects of selective slow wave sleep deprivation in major depression: a high-density EEG investigation,” *J. Psychiatr. Res.*, vol. 45, pp. 1019–1026, Aug. 2011.
- [4] P. Nyström, “The infant mirror neuron system studied with high density EEG,” *Soc. Neurosci.*, vol. 3, no. 3-4, pp. 334–347, 2008.
- [5] J. E. Kline, H. J. Huang, K. L. Snyder, and D. P. Ferris, “Isolating gait-related movement artifacts in electroencephalography during human walking,” *J. Neural Eng.*, vol. 12, p. 046022, Aug. 2015.
- [6] E.-R. Symeonidou, A. D. Nordin, W. D. Hairston, and D. P. Ferris, “Effects of cable sway, electrode surface area, and electrode mass on electroencephalography signal quality during motion,” *Sensors*, vol. 18, Apr. 2018.
- [7] A. Delorme, J. Palmer, J. Onton, R. Oostenveld, and S. Makeig, “Independent EEG sources are dipolar,” *PLoS One*, vol. 7, p. e30135, Feb. 2012.

- [8] T. Mullen, C. Kothe, Y. M. Chi, A. Ojeda, T. Kerth, S. Makeig, G. Cauwenberghs, and T.-P. Jung, “Real-time modeling and 3D visualization of source dynamics and connectivity using wearable EEG,” *Conf. Proc. IEEE Eng. Med. Biol. Soc.*, vol. 2013, pp. 2184–2187, 2013.
- [9] F. Artoni, D. Menicucci, A. Delorme, S. Makeig, and S. Micera, “RELICA: A method for estimating the reliability of independent components,” *Neuroimage*, vol. 103, pp. 391–400, Dec. 2014.
- [10] A. S. Oliveira, B. R. Schlink, W. D. Hairston, P. König, and D. P. Ferris, “Induction and separation of motion artifacts in EEG data using a mobile phantom head device,” *J. Neural Eng.*, vol. 13, p. 036014, June 2016.
- [11] A. D. Nordin, W. D. Hairston, and D. P. Ferris, “Dual-electrode motion artifact cancellation for mobile electroencephalography,” *J. Neural Eng.*, vol. 15, p. 056024, Oct. 2018.
- [12] M. Seeber, L.-M. Cantonas, M. Hoevels, T. Sesia, V. Visser-Vandewalle, and C. M. Michel, “Subcortical electrophysiological activity is detectable with high-density EEG source imaging,” *Nat. Commun.*, vol. 10, p. 753, Feb. 2019.
- [13] T. Hedrich, G. Pellegrino, E. Kobayashi, J. M. Lina, and C. Grova, “Comparison of the spatial resolution of source imaging techniques in high-density EEG and MEG,” *Neuroimage*, vol. 157, pp. 531–544, Aug. 2017.
- [14] S. Klamer, A. Elshahabi, H. Lerche, C. Braun, M. Erb, K. Scheffler, and N. K. Focke, “Differences between MEG and high-density EEG source localizations using a distributed source model in comparison to fMRI,” *Brain Topogr.*, vol. 28, pp. 87–94, Jan. 2015.
- [15] C. J. Scarff, A. Reynolds, B. G. Goodyear, C. W. Ponton, J. C. Dort, and J. J. Eggermont, “Simultaneous 3-T fMRI and high-density recording of human auditory evoked potentials,” *Neuroimage*, vol. 23, pp. 1129–1142, Nov. 2004.

- [16] G. Lantz, R. Grave de Peralta, L. Spinelli, M. Seeck, and C. M. Michel, “Epileptic source localization with high density EEG: how many electrodes are needed?,” *Clin. Neurophysiol.*, vol. 114, pp. 63–69, Jan. 2003.
- [17] B. He and T. Musha, “Effects of cavities on EEG dipole localization and their relations with surface electrode positions,” *Int. J. Biomed. Comput.*, vol. 24, pp. 269–282, Dec. 1989.
- [18] A. Keil, S. Debener, G. Gratton, M. Junghöfer, E. S. Kappenman, S. J. Luck, P. Luu, G. A. Miller, and C. M. Yee, “Committee report: publication guidelines and recommendations for studies using electroencephalography and magnetoencephalography,” *Psychophysiology*, vol. 51, pp. 1–21, Jan. 2014.
- [19] R. N. Kavanagh, T. M. Darcey, D. Lehmann, and D. H. Fender, “Evaluation of methods for Three-Dimensional localization of electrical sources in the human brain,” *IEEE Transactions on Biomedical Engineering*, vol. BME-25, pp. 421–429, Sept. 1978.
- [20] D. Khosla, M. Don, and B. Kwong, “Spatial mislocalization of EEG electrodes – effects on accuracy of dipole estimation,” *Clin. Neurophysiol.*, vol. 110, pp. 261–271, Feb. 1999.
- [21] Y. Wang and J. Gotman, “The influence of electrode location errors on EEG dipole source localization with a realistic head model,” *Clin. Neurophysiol.*, vol. 112, pp. 1777–1780, Sept. 2001.
- [22] L. Beltrachini, N. von Ellenrieder, and C. H. Muravchik, “General bounds for electrode mislocation on the EEG inverse problem,” *Comput. Methods Programs Biomed.*, vol. 103, pp. 1–9, July 2011.
- [23] Z. Akalin Acar and S. Makeig, “Effects of forward model errors on EEG source localization,” *Brain Topogr.*, vol. 26, pp. 378–396, July 2013.

- [24] M. Marino, Q. Liu, S. Brem, N. Wenderoth, and D. Mantini, “Automated detection and labeling of high-density EEG electrodes from structural MR images,” *J. Neural Eng.*, vol. 13, p. 056003, Oct. 2016.
- [25] L. Koessler, L. Maillard, A. Benhadid, J.-P. Vignal, M. Braun, and H. Vespignani, “Spatial localization of EEG electrodes,” *Neurophysiol. Clin.*, vol. 37, pp. 97–102, Apr. 2007.
- [26] M. Rodríguez-Calvache, A. Calle, S. Valderrama, I. A. López, and J. D. López, “Analysis of exact electrode positioning systems for Multichannel-EEG,” in *Applied Computer Sciences in Engineering*, pp. 523–534, Springer International Publishing, 2018.
- [27] L. Engels, N. Warzee, and X. De Tiege, “Method of locating eeg and meg sensors on a head,” Feb. 2013.
- [28] C. C. Cline, C. Coogan, and B. He, “EEG electrode digitization with commercial virtual reality hardware,” *PLoS One*, vol. 13, p. e0207516, Nov. 2018.
- [29] L. Koessler, T. Cecchin, E. Ternisien, and L. Maillard, “3D handheld laser scanner based approach for automatic identification and localization of EEG sensors,” *Conf. Proc. IEEE Eng. Med. Biol. Soc.*, vol. 2010, pp. 3707–3710, 2010.
- [30] U. Baysal and G. Sengül, “Single camera photogrammetry system for EEG electrode identification and localization,” *Ann. Biomed. Eng.*, vol. 38, pp. 1539–1547, Apr. 2010.
- [31] T. Clausner, S. S. Dalal, and M. Crespo-García, “Photogrammetry-Based head digitization for rapid and accurate localization of EEG electrodes and MEG fiducial markers using a single digital SLR camera,” *Front. Neurosci.*, vol. 11, p. 264, May 2017.
- [32] P. M. R. Reis and M. Lochmann, “Using a motion capture system for spatial localization of EEG electrodes,” *Front. Neurosci.*, vol. 9, p. 130, Apr. 2015.

- [33] G. S. Russell, K. Jeffrey Eriksen, P. Poolman, P. Luu, and D. M. Tucker, “Geodesic photogrammetry for localizing sensor positions in dense-array EEG,” *Clin. Neurophysiol.*, vol. 116, pp. 1130–1140, May 2005.
- [34] C. Song, S. Jeon, S. Lee, H.-G. Ha, J. Kim, and J. Hong, “Augmented reality-based electrode guidance system for reliable electroencephalography,” *Biomed. Eng. Online*, vol. 17, p. 64, May 2018.
- [35] “xensor™ | ANT neuro.” <https://www.ant-neuro.com/products/xensor>. Accessed: 2019-2-8.
- [36] “Brainsight TMS navigation - rogue resolutions.” <https://www.rogue-resolutions.com/catalogue/neuro-navigation/brainsight-tms-navigation/>. Accessed: 2019-2-8.
- [37] C. Chen and A. Kak, “Modeling and calibration of a structured light scanner for 3-D robot vision,” in *Proceedings. 1987 IEEE International Conference on Robotics and Automation*, vol. 4 of *Proceedings. 1987 IEEE International Conference on Robotics and Automation*, pp. 807–815, ieeexplore.ieee.org, Mar. 1987.
- [38] A. Delorme and S. Makeig, “EEGLAB: an open source toolbox for analysis of single-trial EEG dynamics including independent component analysis,” *J. Neurosci. Methods*, vol. 134, pp. 9–21, Mar. 2004.
- [39] R. Oostenveld, P. Fries, E. Maris, and J.-M. Schoffelen, “FieldTrip: Open source software for advanced analysis of MEG, EEG, and invasive electrophysiological data,” *Comput. Intell. Neurosci.*, vol. 2011, Dec. 2010.
- [40] G. A. Taberna, M. Marino, M. Ganzetti, and D. Mantini, “Spatial localization of EEG electrodes using 3D scanning,” *J. Neural Eng.*, Jan. 2019.

- [41] S. Vema Krishna Murthy, M. MacLellan, S. Beyea, and T. Bardouille, “Faster and improved 3-D head digitization in MEG using kinect,” *Front. Neurosci.*, vol. 8, p. 326, Oct. 2014.
- [42] J. Zhang, J. Chen, S. Chen, G. Xiao, and X. Li, “Multimodal spatial calibration for accurately registering EEG sensor positions,” *Comput. Math. Methods Med.*, vol. 2014, p. 826019, Apr. 2014.
- [43] G. H. Klem, H. O. Lüders, H. H. Jasper, and C. Elger, “The ten-twenty electrode system of the international federation. the international federation of clinical neurophysiology,” *Electroencephalogr. Clin. Neurophysiol. Suppl.*, vol. 52, pp. 3–6, 1999.
- [44] S. S. Dalal, S. Rampp, F. Willomitzer, and S. Ettl, “Consequences of EEG electrode position error on ultimate beamformer source reconstruction performance,” *Front. Neurosci.*, vol. 8, p. 42, Mar. 2014.
- [45] J. A. Palmer, K. Kreutz-Delgado, B. D. Rao, and S. Makeig, “Modeling and estimation of dependent subspaces with non-radially symmetric and skewed densities,” in *Independent Component Analysis and Signal Separation*, pp. 97–104, Springer Berlin Heidelberg, 2007.
- [46] A. C. Evans, D. L. Collins, S. R. Mills, E. D. Brown, R. L. Kelly, and T. M. Peters, “3D statistical neuroanatomical models from 305 MRI volumes,” in *1993 IEEE Conference Record Nuclear Science Symposium and Medical Imaging Conference*, pp. 1813–1817 vol.3, Oct. 1993.
- [47] N. Moshtagh, “Minimum volume enclosing ellipsoid,” [pdfs.semanticscholar.org](http://pdfs.semanticscholar.org), 2005.
- [48] N. Bigdely-Shamlo, T. Mullen, K. Kreutz-Delgado, and S. Makeig, “Measure projection analysis: a probabilistic approach to EEG source comparison and multi-subject inference,” *Neuroimage*, vol. 72, pp. 287–303, May 2013.

- [49] J. L. Lancaster, M. G. Woldorff, L. M. Parsons, M. Liotti, C. S. Freitas, L. Rainey, P. V. Kochunov, D. Nickerson, S. A. Mikiten, and P. T. Fox, “Automated talairach atlas labels for functional brain mapping,” *Hum. Brain Mapp.*, vol. 10, pp. 120–131, July 2000.
- [50] R. Oostenveld and P. Praamstra, “The five percent electrode system for high-resolution EEG and ERP measurements,” *Clin. Neurophysiol.*, vol. 112, pp. 713–719, Apr. 2001.
- [51] S. Chen, Y. He, H. Qiu, X. Yan, and M. Zhao, “Spatial localization of EEG electrodes in a TOF+CCD camera system,” *Front. Neuroinform.*, vol. 13, p. 21, Apr. 2019.
- [52] S. Homölle and R. Oostenveld, “Using a structured-light 3D scanner to improve EEG source modeling with more accurate electrode positions,” *J. Neurosci. Methods*, p. 108378, July 2019.
- [53] G. Van Hoey, B. Vanrumste, M. D’Havé, R. Van de Walle, I. Lemahieu, and P. Boon, “Influence of measurement noise and electrode mislocalisation on EEG dipole-source localisation,” *Med. Biol. Eng. Comput.*, vol. 38, pp. 287–296, May 2000.
- [54] S. Y. Shirazi and H. J. Huang, “Influence of mismarking fiducial locations on EEG source estimation\*,” in *2019 9th International IEEE/EMBS Conference on Neural Engineering (NER)*, pp. 377–380, Mar. 2019.
- [55] Z. Akalin Acar, C. E. Acar, and S. Makeig, “Simultaneous head tissue conductivity and EEG source location estimation,” *Neuroimage*, vol. 124, pp. 168–180, Jan. 2016.
- [56] K. Mahjoory, V. V. Nikulin, L. Botrel, K. Linkenkaer-Hansen, M. M. Fato, and S. Haufe, “Consistency of EEG source localization and connectivity estimates,” *Neuroimage*, vol. 152, pp. 590–601, May 2017.
- [57] J. Song, C. Davey, C. Poulsen, P. Luu, S. Turovets, E. Anderson, K. Li, and D. Tucker, “EEG source localization: Sensor density and head surface coverage,” *J. Neurosci. Methods*, vol. 256, pp. 9–21, Dec. 2015.

- [58] L. Beltrachini, “Sensitivity of the projected subtraction approach to mesh degeneracies and its impact on the forward problem in EEG,” *IEEE Trans. Biomed. Eng.*, vol. 66, pp. 273–282, Jan. 2019.
- [59] A. Bradley, J. Yao, J. Dewald, and C.-P. Richter, “Evaluation of electroencephalography source localization algorithms with multiple cortical sources,” *PLoS One*, vol. 11, p. e0147266, Jan. 2016.
- [60] Z. A. Acar and S. Makeig, “Neuroelectromagnetic forward head modeling toolbox,” *J. Neurosci. Methods*, vol. 190, pp. 258–270, July 2010.

## **CHAPTER 3: Influence of Mismarking Fiducial Locations on EEG Source Estimation**

### Introduction

Digitizing electrode locations is an essential step for setting up a head model to estimate cortical and subcortical sources from magneto-/electro-encephalography (M/EEG) signals [1]. The digitizing process involves recording three-dimensional positions of the M/EEG electrodes in a global coordinate system and transforming the locations from the global coordinates to the head coordinate system. This transformation requires that the two coordinate systems share at least three anatomical landmarks (i.e. fiducials). The fiducials are typically the left preauricular, right preauricular, and nasion [1, 2].

After digitizing the 3D locations of the fiducials and electrodes, these locations are warped to a head model or vice versa [3]. For studies that involve concurrent tomographic imaging such as magnetic resonance imaging (MRI), digitization, transformation to the head coordinate system, and warping to the head model can be made simultaneously [4], but for other studies, digitized locations must be manually coregistered to construct the head model [1]. Therefore, digitizing can significantly affect the ability to achieve a realistic head model and estimations of source locations [3].

To our knowledge, only a couple of studies examined the effects of digitizing errors on source estimation, and outcomes of these studies do not seem consistent. Beltachini and colleagues [5] suggested that effects of electrode mislocations are negligible on the estimated source locations, while Dalal et al. [6] showed that quality of the output signal degrades significantly with higher uncertainties in the electrode digitization. We did not find any published study that examined the possible effects of mismarking fiducial locations on source estimation.

The purpose of this study was to analyze changes in the estimated source location as a result of shifting the fiducial locations to simulate mismarking of the fiducials. We hypothesized that changes in the locations of the fiducials would have a significant effect on the dipole fitting process and source localization.

## Methods

We fitted a mannequin head with a 128-electrode BioSemi (BioSemi B.V., Amsterdam, the Netherlands) cap and digitized the locations of the electrodes and fiducials (left preauricular, LPA; right preauricular, RPA; and nasion, Nz) using an OptiTrack 22-camera motion capture system and a digitizing probe (NaturalPoint Inc., Corvallis, OR). The average ( $\pm$ SD) reliability of this digitization method was  $<1.50 \pm 0.3$  mm for digitizing the mannequin head five times.

To define the head coordinate system, we assumed the LPA and RPA were on the X-axis, and Nz was on the Y-axis (Figure 3.1A). The origin of the head coordinate system was located at the projection of Nz to the X-axis. The Z-axis was defined as the cross product of the X and Y unit vectors and began from the origin. We transformed the digitized electrode locations of the mannequin head to the head coordinate system and used this set of electrodes as the baseline.

To create multiple sets of electrode locations with various fiducial locations, we shifted one fiducial at a time, in 1 mm increments, up to  $\pm 20$  mm in the Y and then the Z directions for the preauriculars, RPA and LPA, and in the X and then the Z directions for the nasion, Nz. This process resulted in 12 fiducial shifts per 1 mm increment (3 fiducials  $\times$  four directions), totaling 240 sets of electrode locations (12 fiducial shifts per 1 mm increment  $\times$  20 fiducial shift increments).

Digitization post-processing and the subsequent analyses throughout the study were performed using MATLAB version 9.4 (R2018a, Mathworks Inc., Natick, MA) and EEGLAB [7] version

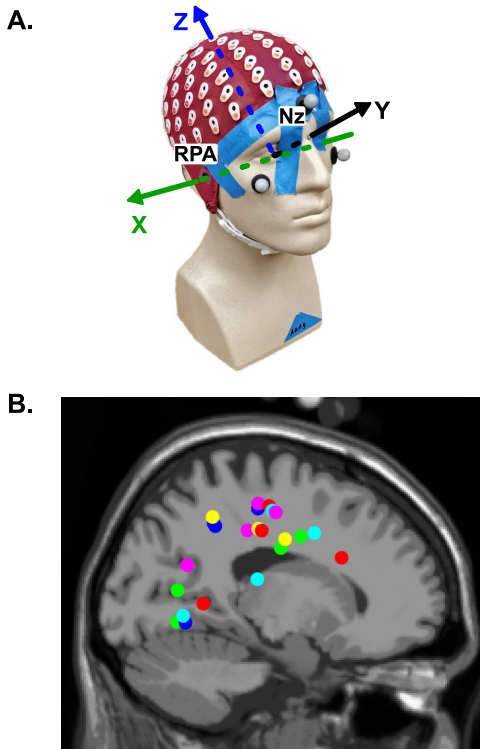


Figure 3.1: **A.** The mannequin head used for digitization with a representation of the head coordinate system. Right preauricular (RPA) and nasion (Nz) are labeled in the picture. **B.** The baseline dipole locations of the 23 independent components (ICs) from a separate study but estimated with the mannequin head digitization rather than the individual subject digitizations using ultrasound. These ICs were used to analyze the influence of the systematic fiducial shifts on the dipole locations.

14.1.2. We used just the fiducial locations to warp the locations of the electrodes and fiducials to the Montreal Neurological Institute's template head model.

#### *Source Estimation and Dipole Fitting*

We used a single representative EEG dataset and weightings of a single Adaptive Mixture Independent Component Analysis (AMICA) from a separate study to perform dipole fitting using the multiple sets of electrode locations with the systematic shifts of the fiducial locations. This repre-

sentative EEG dataset and ICA had 89 independent components, ICs. We used the DIPFIT toolbox version 2.3 to fit dipoles to the ICs. We visually inspected for dipoles with residual variances <15% that stayed inside the brain area across every fiducial shifts, which resulted in total 23 remaining ICs (Figure 3.1B). We analyzed the influence of the fiducial shifts on all twenty-three ICs but picked three to illustrate dipole location alterations in detail: 1) the anterior cingulate, 2) the primary somatosensory cortex, and 3) the premotor cortex. Previous studies have shown that these three areas are active in locomotion and error monitoring [8, 9].

### *Dipole Uncertainty Analysis*

We defined the baseline set of dipoles as the dipoles produced using the baseline locations for the fiducials and electrodes (i.e. no shifts). Each set of electrode locations based on a shifted fiducial produced a new set of dipoles. There were 240 sets of electrode locations resulting in 240 sets of dipoles around the baseline dipole. We considered that the spread or size of the cluster of dipoles was representative of the uncertainty related to the resulting dipole locations.

We quantified dipole uncertainty as the volume of a set of tetrahedrons formed from connecting the 12 dipoles created by shifting every fiducial in 1-mm step in every direction (three fiducials  $\times$  4 direction/fiducial). We identified the outside boundary of the 12-dipole clusters and created the tetrahedrons using MATLAB's `convexHull` function.

We also calculated the maximum dipole cluster width between the dipoles with equidistant fiducial shifts (i.e. the same 12 dipoles used for creating tetrahedrons). Since the tetrahedral volumes did not have similar shapes at each fiducial shift, we formed equivalent rectangular cubes with volumes equal to the tetrahedral volumes and the width equal to the maximum cluster width. Hence, for the equivalent rectangular cubes,  $V = D \times E^2$ , where  $V$  is the tetrahedral volume, which is also the equivalent cube's volume,  $D$  is the maximum cluster width that forms the cube's width, and  $E^2$  is

the cross-sectional area of the cube.

We used step-wise polynomial fits to model the relationship between the uncertainty volume and the fiducial shift distance, and the maximum dipole cluster width and the fiducial distance.

### *Random Fiducial Mismarkings*

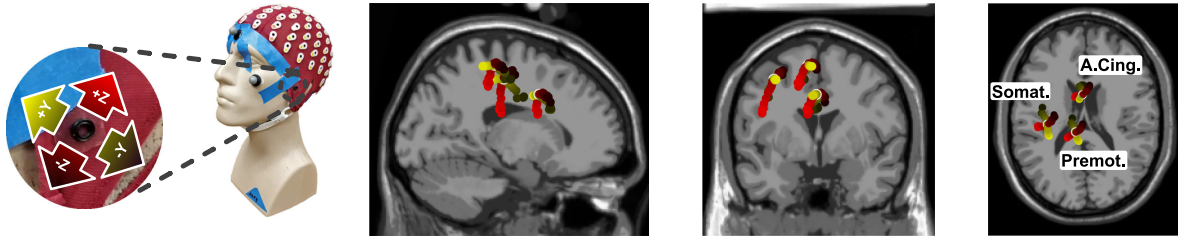
Creating random combinations of fiducial shifts is another approach to analyze the effects of fiducial mismarkings. We generated 100 electrode location datasets for every 1-mm increment of the random fiducial mismarking combinations, producing 2000 datasets (100 datasets/increment  $\times$  20 increments = total 2000 datasets). Each one-hundred mismarkings resided on a circular path with a fixed radius ( $1 \leq r \leq 20$  mm) away from the fiducial baseline locations. We ran DIPFIT using each dataset and compared the results with the outcomes of the systematic fiducial shifts.

## Results

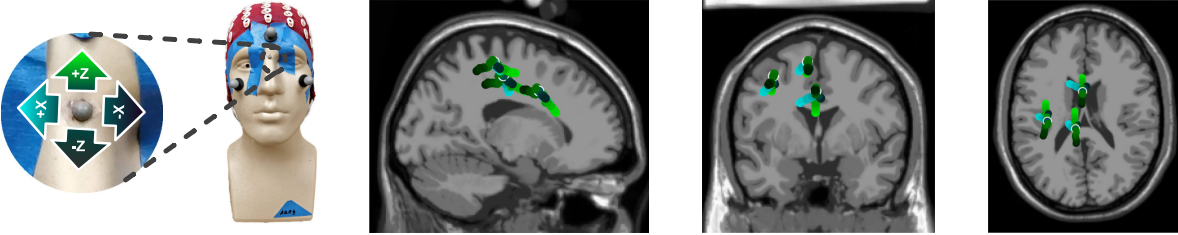
Shifting LPA, Nz, and RPA in different increments and directions resulted in dipole locations that had curvilinear paths in different planes. Each shift direction created changes in similar directions for the dipoles of the three ICs but with different magnitudes (Figure 3.2).

The uncertainty volume increased quadratically as a function of the magnitude of the fiducial shifts ( $r^2 = 0.920$ , Figure 3.3A). The uncertainty volume was  $\sim 0.06\text{ cm}^3$  for fiducial shifts up to 0.5 cm for every IC. For fiducial shifts up to 1.3 cm, all three ICs showed similar increases in uncertainty volumes to  $0.5\text{ cm}^3$ . With fiducial shifts  $>1.3$  cm, the uncertainty volume of all ICs, including the three ICs of interest, began to separate from one another. At a 2 cm shift in fiducials, the average uncertainty volume was  $>2\text{ cm}^3$ .

**A. variation in the left preauricular**



**B. variation in the nasion**



**C. variation in the right preauricular**

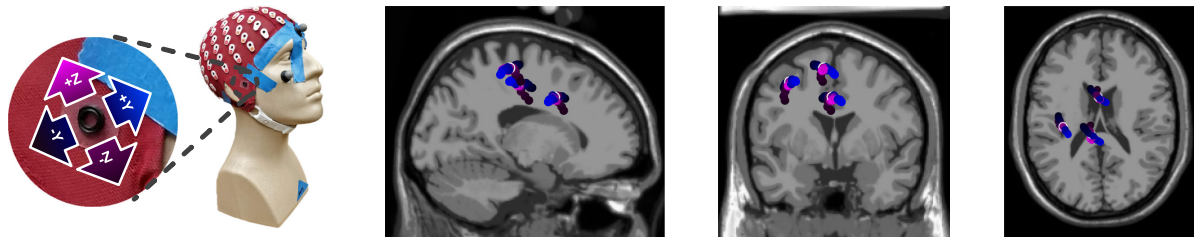
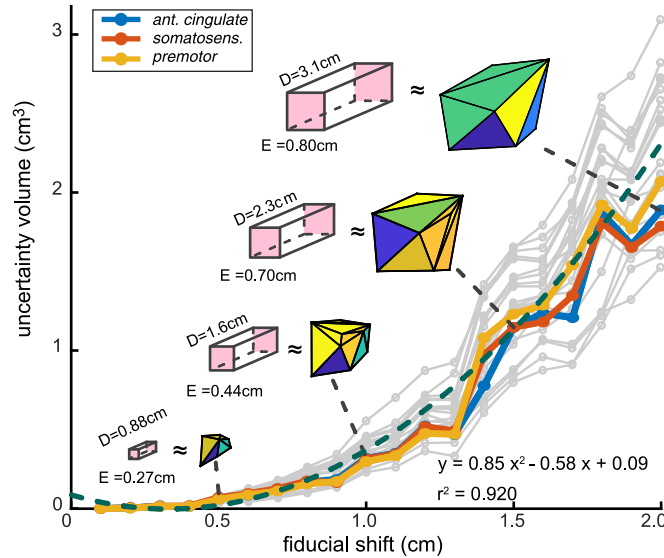


Figure 3.2: Fiducial mislocations and their corresponding estimated dipoles for **A.** Left preauricular (LPA), **B.** Nasion (Nz) and **C.** Right preauricular (RPA) for three independent components (ICs). Dipoles are located at the anterior cingulate (A.Cing.), the primary somatosensory cortex (Somat.) and at the premotor cortex (Premot.). Lighter colors show positive direction for the fiducial shifts. For each fiducial, resultant dipoles are plotted in sagittal, frontal and top views.

The maximum dipole cluster width for an IC had a linear relationship with the fiducial shifts ( $r^2 = 0.79$ , Figure 3.3B). The average maximum cluster width exceeded 1 cm for shifts greater than 0.5 cm and was  $\sim 4$  cm for fiducial shifts of 2 cm. Some of the cluster widths of different ICs started to deviate from the linear fit for the fiducial shifts  $> 0.5$  cm, although, we did not observe similar trend for the uncertainty volumes. The dipole located in the primary somatosensory cortex had larger maximum distances than the ICs in the anterior cingulate and premotor cortex for fiducial shifts greater than 1.3 cm.

**A. uncertainty volume due to fiducial shifts**



**B. maximum dipole cluster width due to fiducial shifts**

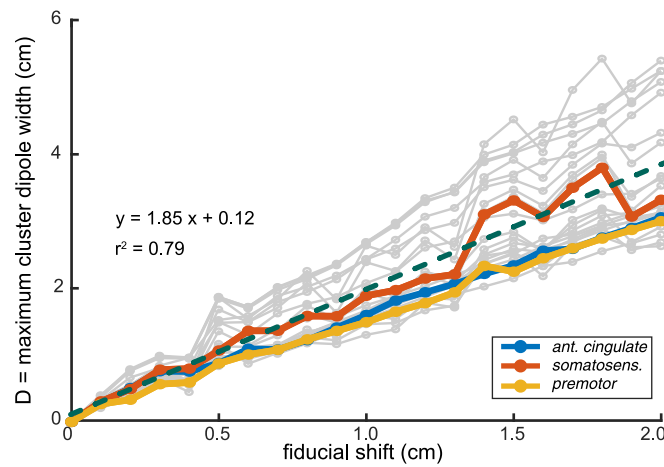


Figure 3.3: **A.** Relationship between the uncertainty volume and fiducial shifts. ICs in Figure 3.2 are drawn in color: anterior cingulate (ant. cingulate), somatosensory cortex (somatosens.) and premotor cortex (premotor). Tetrahedrons represent dipole uncertainty at the anterior cingulate. Pink cubes has the same volume as the tetrahedral volumes, with the same width as the maximum cluster width (D). The green dashed line quadratically models the uncertainty volume as a function of the fiducial shift. **B.** Maximum cluster width (D) of the dipoles estimated from the equidistant fiducial shifts. The green dashed line relates the maximum cluster width to the fiducial shift.

Comparing results of the random fiducial mismarking combinations and the tetrahedral volumes from the systematic fiducial shifts, we found that 1) For each 1-mm increment, no random com-

bination of the fiducial shifts (out of 100) could cancel out the effects of the shifts and result in a dipole that could make the uncertainty volume or cluster width smaller, and 2) >95% of the dipole estimations with random fiducial mismarking combinations at each 1-mm increment were in a close proximity of the corresponding tetrahedral surface (within ~20% of the maximum cluster width).

### Discussion and Conclusion

This study revealed the relationship of fiducial mismarkings during electrode digitization on the subsequent uncertainty of dipole location estimation. We found that shifts of a single fiducial location up to 0.5 cm resulted in an uncertainty volume  $<0.06 \text{ cm}^3$  and a maximum distance  $<1 \text{ cm}$ . When fiducial shifts were greater than 1.3 cm, dipole location uncertainty increased to  $>1 \text{ cm}^3$  and the maximum distance increased to  $>2 \text{ cm}$ .

One interesting finding was that the largest maximum distances, among the three ICs of interest, occurred in the primary somatosensory cortex, which is an area frequently discussed in the EEG studies related to walking [8,9]. A previous study found that tangential sources near the boundary of the cortex were more sensitive to electrode location errors, which could explain the larger maximum distances for the dipole at the primary somatosensory cortex compared to a dipole deeper within the cortex such as the anterior cingulate [5].

Another interesting finding was that the linear fiducial shifts mapped to curvilinear dipole paths in different planes, which allowed the use of superposition to estimate dipole uncertainties created from fiducial mismarking combinations. Fiducial mismarking combinations are less likely to cancel each other, since the mismarking directions map to dipole paths in different planes. Fiducial mismarking combinations also created dipole spreads close to the uncertainty volumes that the systematic fiducial shifts had predicted.

Dipole cluster width was more sensitive to the fiducial shifts compared to volumetric uncertainty. Dipole cluster width had a steep linear relation with the fiducial shifts and mismarking the fiducials could change the location of a dipole as much as twice the fiducial mismarking shift. A recent study found that the reliability of a widely-used electromagnetic electrode digitizing system was  $\sim$ 0.8 cm [10]. Hence, even with perfect markings of the fiducials, there will still be up to 1.5 cm (17% of the head radius) uncertainty for the estimated dipole locations, just as a result of the reliability of the digitizing device.

Limitations of this study were that we did not examine every combination of the fiducial mismarkings and that we only co-registered the fiducials with the MNI head model for warping the electrode locations to the head model. While examining every combination of fiducial mismarkings was not practical, an advantage of analyzing random combinations of the fiducial mismarkings with the same distance from the baseline was that this approach could be used to estimate the mismarking effects for multiple digitizing systems if the digitizing reliability is known. While we could have co-registered more electrodes to the MNI head model, this would lose the individual characteristics of the digitized head. Alternatively, EEGLAB's NFT toolbox enables warping of the MNI head model to all of the digitized electrode locations [11], but coupling NFT with 240 incremental electrode-location datasets was beyond our computational capacity.

Based on our results, we recommend using a digitizing system with measurement errors less than 0.5 cm and marking the fiducials within 0.5 cm of the actual fiducial to avoid errors greater than 1.5 cm in dipole location. Future work will compare the reliability of different digitizing systems to determine which digitizing systems have measurement errors less than the recommended 0.5 cm. While digitizing the actual locations of the EEG electrodes should provide greater dipole specificity, this study showed that small fiducial mismarkings could result in large dipole location uncertainty. To reduce dipole location uncertainty, care should be taken to minimize the cumulative potential errors from the user mismarking fiducial locations during the digitization process and the

measurement errors from the digitization system.

## References

- [1] L. Koessler, L. Maillard, A. Benhadid, J.-P. Vignal, M. Braun, and H. Vespignani, “Spatial localization of EEG electrodes,” *Neurophysiol. Clin.*, vol. 37, pp. 97–102, Apr. 2007.
- [2] M. Fuchs, M. Wagner, and J. Kastner, “Development of volume conductor and source models to localize epileptic foci,” *J. Clin. Neurophysiol.*, vol. 24, pp. 101–119, Apr. 2007.
- [3] Z. Akalin Acar and S. Makeig, “Effects of forward model errors on EEG source localization,” *Brain Topogr.*, vol. 26, pp. 378–396, July 2013.
- [4] M. Marino, Q. Liu, S. Brem, N. Wenderoth, and D. Mantini, “Automated detection and labeling of high-density EEG electrodes from structural MR images,” *J. Neural Eng.*, vol. 13, p. 056003, Oct. 2016.
- [5] L. Beltrachini, N. von Ellenrieder, and C. H. Muravchik, “General bounds for electrode mislocation on the EEG inverse problem,” *Comput. Methods Programs Biomed.*, vol. 103, pp. 1–9, July 2011.
- [6] S. S. Dalal, S. Rampp, F. Willomitzer, and S. Ettl, “Consequences of EEG electrode position error on ultimate beamformer source reconstruction performance,” *Front. Neurosci.*, vol. 8, p. 42, Mar. 2014.
- [7] A. Delorme and S. Makeig, “EEGLAB: an open source toolbox for analysis of single-trial EEG dynamics including independent component analysis,” *J. Neurosci. Methods*, vol. 134, pp. 9–21, Mar. 2004.

- [8] T. P. Luu, J. A. Brantley, S. Nakagome, F. Zhu, and J. L. Contreras-Vidal, “ELECTROCORTICAL correlates of human level-ground, slope, and stair walking,” *PLoS One*, vol. 12, p. e0188500, Nov. 2017.
- [9] S. M. Peterson and D. P. Ferris, “Differentiation in theta and beta electrocortical activity between visual and physical perturbations to walking and standing balance,” *eNeuro*, vol. 5, July 2018.
- [10] T. Clausner, S. S. Dalal, and M. Crespo-García, “Photogrammetry-Based head digitization for rapid and accurate localization of EEG electrodes and MEG fiducial markers using a single digital SLR camera,” *Front. Neurosci.*, vol. 11, p. 264, May 2017.
- [11] Z. A. Acar and S. Makeig, “Neuroelectromagnetic forward head modeling toolbox,” *J. Neurosci. Methods*, vol. 190, pp. 258–270, July 2010.

## **CHAPTER 4: Influence of Mismarking Fiducial Locations on EEG Source Estimation**

### Introduction

Perturbing locomotion often produces error-driven adaptation where subjects adjust their locomotor patterns to reduce errors, but these adjustments revert to the unperturbed patterns after the perturbations are removed (i.e. wash-out) [1]. When subjects are re-exposed to the same perturbations or exposed to new perturbations, they adapt faster and may also modify unperturbed locomotor patterns [2]. However, these modifications may not transfer across lower limbs according to a split-belt walking study [3]. Despite the wash-out often seen with error-driven adaptation, split-crank cycling and split-belt walking can result in retained post-perturbation modifications if the modifications were not the direct task goals [4, 5]. For example, after cycling with different crank angles, subjects had perturbation-specific muscle activation patterns which did not wash-out post-perturbation [4]. These locomotor behaviors indicate that perturbations indeed modify locomotor responses beyond the perturbation period and that tuning perturbation features could modulate locomotor responses. Determining motor and cortical responses to different perturbations during a variety of locomotor tasks, beyond just walking, could greatly improve the understanding of locomotor adaptation processes.

Advancements in brain imaging technologies such as high-density electroencephalography (EEG), functional magnetic resonance imaging, and positron emission tomography have helped researchers identify supra-spinal correlates of locomotion [6–8]. The anterior cingulate cortex theta (3-8 Hz) power increases significantly during double-support in walking and during extension-onset in recumbent stepping [9, 10]. These studies suggest that the anterior cingulate activity may be

monitoring more demanding locomotion phases. The supplementary motor area (SMA) has similar theta power fluctuations during walking, cycling, and recumbent stepping [6, 10, 11]. In general, the SMA and the motor cortex exhibit substantial alpha-beta (8-30 Hz) fluctuations during walking, with decreased alpha-beta power indicating active processing in the motor cortex [12].

The anterior cingulate cortex and SMA also both strongly respond to perturbations during walking and standing. Previous studies on split-belt walking, perturbed beam walking, walking over obstacles, and perturbed stepping reported perturbation-elicited activity of anterior cingulate, SMA, or in both areas [8,9,13–16]. The anterior cingulate cortex (or the equivalent mid-prefrontal cortex in the EEG channel studies) activity is often associated with error monitoring or motor learning, while SMA activity is associated with sensorimotor integration [15,17,18]. If the anterior cingulate cortex has an error monitoring function, we expect that the activity would scale with the error size [19]. If the anterior cingulate has a role in motor learning, we expect the activity would decrease with more perturbation experience. Previous studies on walking over obstacles and perturbed standing did not observe decreased anterior cingulate activity with more experience [13,20]. On the other hand, a recent study reported scaling of central midline EEG signals at the Cz electrode with balance performance during a perturbed standing task [21]. However, all three studies had insufficient spatial resolution to determine confidently whether the electrocortical dynamics were from a single functional cortical area.

The purpose of this study was to determine the electrocortical signatures of motor responses to perturbations during a seated locomotor task. Adding perturbations during seated locomotor tasks such as recumbent stepping, which likely shares neural control with walking [22,23] could provide an alternative option for gait rehabilitation since subjects do not need to maintain their balance. Using our motorized recumbent stepper [24], we applied discrete mechanical perturbations during each stride and also had intermittent no-perturbation "catch" strides. The catch strides could probe whether subjects were updating anticipatory motor control strategies.

We had four hypotheses. The first hypothesis was that perturbations would initially create motor errors and increase anterior cingulate theta power near the perturbation event. As subjects gained more experience with perturbations, motor errors, and anterior cingulate theta power would decrease. The second hypothesis was that motor errors during the no-perturbation catch strides would increase the more subjects expected to encounter perturbations and that anterior cingulate spectral fluctuations would decrease in the later catches. The third hypothesis was that mid-extension perturbations, when the limbs were moving the fastest, would produce more significant errors and anterior cingulate theta power than extension-onset perturbations. We also expected to identify activity of the left and right motor cortices [10, 11] and hypothesized that spectral power fluctuations of the left and right motor cortices in response to the perturbations would be lateralized.

## Methods

Subjects (n=17, 11 females, age  $25 \pm 4.9$  years) performed perturbed arm-leg stepping on a one degree-of-freedom recumbent stepper (TRS 4000; NuStep, Inc., Ann Arbor, MI) integrated with a servomotor (Kollmorgen, Radford, VA), described in [24] (Figure 4.1a). The mechanically coupled left handle and right pedal move together out of phase with the mechanically coupled right handle and left pedal. As such, subjects could use any combination of their arms and legs to drive the stepper.

### *Experiment procedure and motor errors*

The Institutional Review Board of the University of Central Florida approved the protocol and consent form, and the study was conducted per the principles stated in the Declaration of Helsinki. All subjects gave their written informed consent before starting the experiment. Subjects were

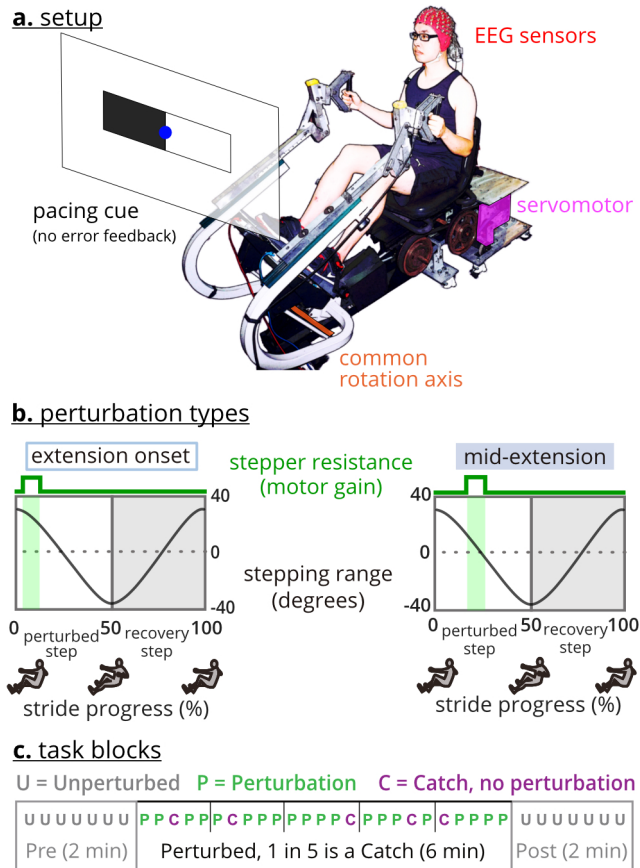


**Figure 4.1: Recumbent stepper and perturbations.** **a.** The recumbent stepper is a one-degree-of-freedom arm-leg exercise device. **b.** Perturbations were applied either at the extension-onset or mid-extension of the targeted leg. Perturbations were increased stepping resistance for 200 milliseconds. **c.** The experiment included four tasks. Each task had three ordered blocks, pre, perturbed stepping, and post. The perturbed stepping block also included random no-perturbation catch strides.

all right-handed, based on the hand they would use to pick an object from the floor. Subjects self-reported no prior neurological or musculoskeletal problems in the past two years before the data collection date.

We recorded EEG using a 128-electrode EEG system (ActiveTwo, BioSemi B.V., Amsterdam, the Netherlands). After placing the EEG cap on the subject's head according to the BioSemi guidelines,

we digitized the electrodes and fiducial locations using an infrared 3D scanner (Structure Sensor, Occipital Inc., Boulder, CO). We ensured that the resistance between the scalp and each electrode was <20 Ohms, indicating good contact between the electrodes and the scalp. We restrained cable movement using a cable holder behind the subject's head and instructed subjects to keep their head steady to reduce EEG cable sway artifacts [25]. We strapped subjects' feet to the pedals after they sat on the stepper seat. We also adjusted the handles to ensure that subjects were comfortable using the handles to drive the stepper.

The stepper's servomotor perturbed the stepping motion with brief 200 ms increases in resistance at either the onset or middle of extension of the target (left or right) leg during the stepping stride (Figure 4.1b). The increased resistance magnitude during a perturbation required 3x the torque to maintain the stepping pace of 60 steps per minute. In total, there were four perturbation types (left/right leg \* mid-extension/extension onset). A pacing cue equal to 60 steps per minute (=30 strides per minute) was provided on a visual display to help subjects maintain similar stepping speeds during and across tasks.

EEG was recorded at 512 Hz using the BioSemi software program, and the stepping kinematics were recorded using the servomotor's encoder at 100 Hz in the stepper program. When the stepper program began and ended, a trigger signal was sent to start and stop the EEG recording to synchronize the data.

#### *Data collection*

The data collection began with two minutes of quiet sitting, during which the pacing cues were shown as EEG was recorded. After completing this quiet sitting portion, subjects completed four 10-minute perturbed stepping tasks in a pseudo-randomized order. Each task only included one perturbation type. For each task, there were three ordered *blocks*: 1) **pre**: two minutes of

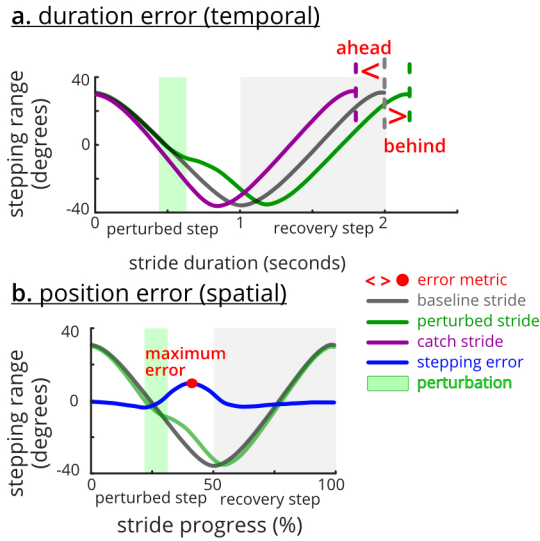


Figure 4.2: **Motor error metrics.** Subjects were instructed to match the pace and step smoothly. **a.** Stepping duration (i.e., temporal) error is the difference between stride duration and the two-second pacing cue. **b.** Stepping position (i.e., spatial) error is the maximum difference between the time-normalized stepping profile and the averaged *pre* profile.

unperturbed stepping, 2) **perturbed stepping**: six minutes of a single perturbation timing, and 3) **post**: two minutes of unperturbed stepping (Figure 4.1c). There were no pauses between blocks. In addition to perturbed strides, the perturbed stepping block included random one-in-five “catch” strides where no perturbation was applied. In this paper, we use pre and pre-perturbation and post and post-perturbation interchangeably. There was two minutes of quiet sitting at the end of the data collection.

Before starting each task, we instructed subjects to **A)** step smoothly as if they were walking, **B)** use both their arms and legs to drive the stepping motion, and **C)** follow the pacing cues that were projected in front of them (Figure 4.1a). We did not instruct subjects on how to follow the pacing cues as there are several options, such as having a leg be at full extension when the rectangle on the same side as the leg was black. Subjects also received no explicit feedback on whether they were stepping faster or slower than the pacing cue. Subjects were given at least two minutes of practice

with the pacing cues before starting the data collection.

### *Stride events*

After importing stepping data into MATLAB (R2018b, MathWorks Inc, Natick, MA), we separated each task into blocks and strides. We defined the strides as the time from one extension-onset of the perturbed leg to the next extension-onset of the perturbed leg. We excluded any incomplete strides. For each stride, we identified the following *events*: perturbed-step extension onset, perturbation (start time), recovery-step extension onset, and the end of the stride. We artificially added perturbation events to the unperturbed strides (i.e., pre, post, and catch strides), equal to the average latency of the perturbation events.

### *Motor errors*

We quantified a temporal (pacing) error and a spatial (stepping) error, from the stepping kinematics (Figure 4.2). In our tasks, subjects should have completed a stride in two seconds based on the 60 steps-per-minute pacing cues. We defined temporal error as the stepping duration error, which was the difference between each stride duration and the two seconds (Figure 4.2a). Since we instructed subjects to step smoothly, we expected the stepping profiles to be smooth and rhythmic during the pre-perturbation block. We defined spatial error as a stepping position error, which was the maximum difference between the time-normalized stepper position profile during each stride and the averaged pre-perturbation stepping profile (Figure 4.2b). We used the servomotor encoder data to quantify the angular stepping position around the stepper's common rotating axis (Figure 4.1a).

## EEG processing

EEG data were analyzed in MATLAB (R2018b, MathWorks Inc, Natick, MA) using a customized pipeline based on EEGLAB (version 2019.0) functions [26] (Figure 4.3). We used a high-pass filter at 1 Hz and a 60 Hz line-noise filter (CleanLine) to minimally clean the raw data [27, 28]. We imported stride events from the synchronized stepping data and concatenated data from all tasks into a single file. We then used a template correlation rejection method to identify and exclude channels with large cyclic artifacts [29].

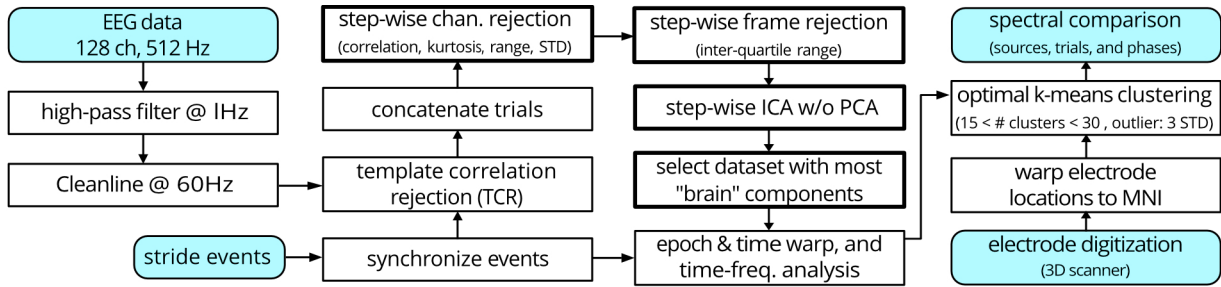


**Figure 4.3: EEG post-processing workflow with a novel step-wise algorithmic parameter sweeping noise rejection process.** Shaded blocks indicate inputs or outputs. Thick lined blocks highlight the novel step-wise rejection approach.

We developed and used a novel step-wise channel and frame rejection algorithm to reject channels and data frames that still contained considerable noise (Figure 4.3). We removed the researcher's need to set single thresholds for the channel and frame rejection steps. Instead, the step-wise algorithm identified a suite of thresholds, from lenient to conservative, that created 32 separate datasets with different rejection levels for each participant (8 steps for channel rejection \* 4 steps for data-frame rejection = 32 datasets). Channel rejection metrics were the signal range, standard deviation, kurtosis, and correlation to the other channels. Frame rejection involved finding periods of the EEG data with a significantly higher signal variability than the overall median of signal variability. While the number of the rejected channels and frames varied for each participant and

increment, we set the rejection thresholds such that the most conservative increment always retained  $> 85$  channels and  $> 80\%$  of data.

We used independent component analysis (ICA), the dipolar source estimation technique (DIPFIT), and a multi-variate source classifier (ICLabel) on each step-wise dataset to identify and locate the sources that contributed to the EEG signals. We specifically used the adaptive mixture independent component analysis (AMICA) to separate the EEG into temporally independent components [30]. To select the best increment from the 32 step-wise datasets, we first estimated the source locations for each dataset's independent components using EEGLAB's DIPFIT version 3.0. We then excluded any source located outside the brain or with the residual variance  $> 15\%$ . We then used EEGLAB's ICLabel toolbox to classify the source types as "brain" or "non-brain" [31] and selected the step-wise dataset with the topmost "brain" sources as the representative dataset for each subject. We visually checked the results of the ICLabel for the selected dataset to confirm the classification of the sources as "brain" (or "non-brain").

We then clustered the sources across all subjects based on the source location, power spectrum, and scalp map. We divided the power spectrum and scalp map into ten bins. The binned power spectrum was from 3 to 25 Hz. The Laplacian of the scalp map was used for clustering [32]. We developed and used a novel optimal k-means approach to determine the number of clusters from a range of possible numbers of clusters provided to the algorithm (here, from 15 to 30 clusters). The optimal k-means approach uses MATLAB's "evalcluster" function to find the specific number of clusters that maximize the similarity of the sources within each cluster. We kept and analyzed only the clusters that contained components from more than 70% of the subjects. If a subject had multiple sources in a cluster, we only kept the source with the largest channel data variance. We identified Brodmann Areas and cortical cortices of the sources and cluster centroids using Talairach coordinates and talairach.org [33, 34].

We computed the time-frequency spectral power of each source in the cluster across the stride epochs, known as event-related spectral perturbations (ERSP) [35]. For hypotheses 1, 2, and 4, each epoch was a stride, and for hypothesis 3, each epoch was  $-400$  ms to  $+400$  ms of the perturbation event. We padded the epochs by 700 ms to avoid possible edge effects. Next, we baseline-normalized the spectral power based on the pre-perturbation block's average spectral power and computed the ensembled average ERSPs across subjects. We determined the significant event-related synchronization and event-related desynchronization across the ERSPs using EEGLAB's bootstrapping method with alpha set at 0.05 [36]. ERSP images only show significant spectral fluctuations.

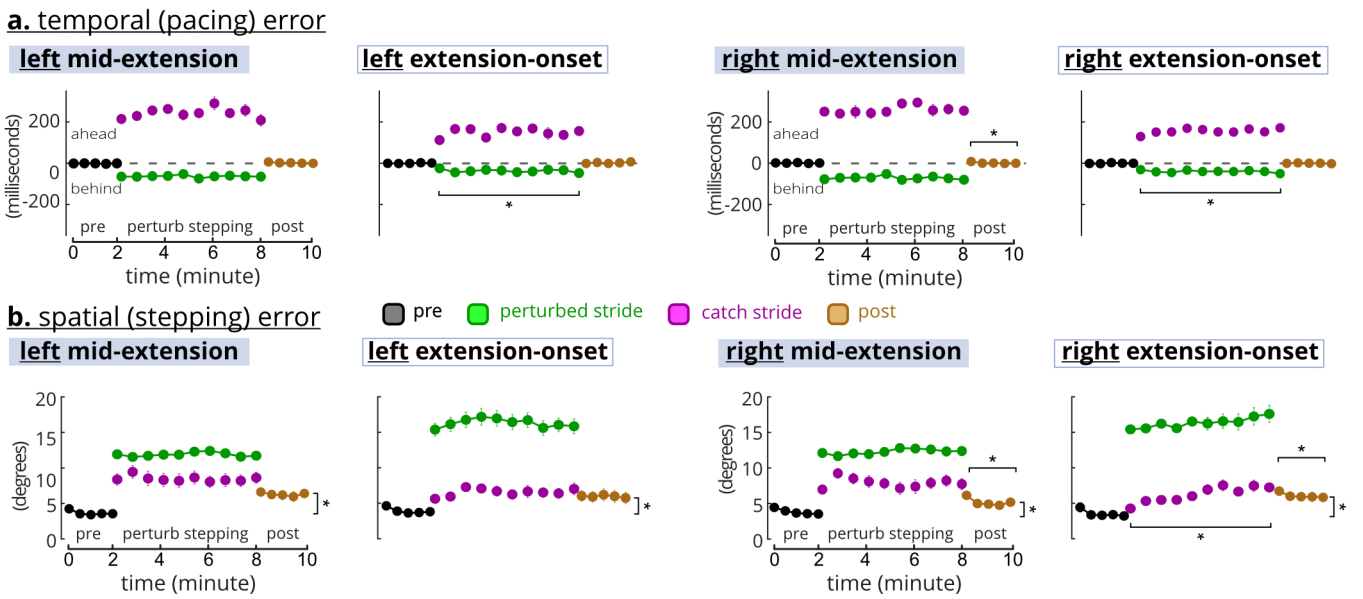


**Figure 4.4: Temporal and spatial errors during perturbed stepping.** The *perturbed-stepping* block include both perturbed strides (green) and one-in-five random catch strides (purple). For *perturbed-stepping*, the 10 circles are the averages of 10% batches. For *pre* and *post*, the 5 circles are the averages of 20% batches. \* indicates significant post-hoc LSD tests. **a.** Temporal errors were different between perturbed and catch strides ( $\sim 50$  ms vs  $\sim 200$  ms) and returned to the *pre* levels during the *post* block. **b.** Spatial error was greater for the perturbed strides than catch strides, and did not return to *pre* levels during *post*.

## *Statistical analysis*

### *Identification of motor responses*

We tested the temporal and spatial errors to determine the error behavior. For each subject, we divided their strides into 20% batches in the pre and post blocks and 10% batches in the perturbed-stepping block [37]. We compared the average of the first and last batches of perturbed strides, catch strides, and post-perturbations strides, as well as the last batch of pre-perturbation strides using repeated-measure analysis of variance (rANOVA) for each error and task. If the rANOVA was significant, we performed a priori Fisher's Least Significant Difference (LSD) tests for the following pairs: 1) late pre vs. late post (for sustained post modifications and wash-out), 2) early vs. late post (for wash-out), 3) early vs. late catch (for adaptation), and 4) early vs. late perturbed (for adaptation). The significance level for all statistical tests was 0.05.

### *Tests for hypotheses 1 and 2: adaptation of motor and cortical responses*

We compared motor errors and electrocortical dynamics between the early (first 33% of the strides) and late (last 33% of the strides) in the perturbed stepping block. Here, we used 33% of the strides as early or late to retain at least 10 strides per subject (total perturbed strides $\approx$ 140-150, total catch strides $\approx$ 30-40) for EEG group-level analyses [35, 36]. We tested motor errors for the perturbed and catch strides separately and used rANOVA with three factors: 1) *adaptation* with two levels: early and late, 2) *task side* with two levels: left and right, and 3) *perturbation timing* also with two levels: mid-extension and extension-onset. We performed post-hoc Student paired t-tests only if the adaptation had a significant main effect because adaptation was the only factor pertinent to our first two hypotheses. To compare the electrocortical responses between early and late perturbed strides and early and late catch strides, we computed the spectral fluctuations and averaged the

spectral powers to derive the theta-band (3-8 Hz) ERSP waveform [36, 38]. We compared the early and late theta-band average ERSP waveforms using bootstrapped paired t-tests and false discovery rate corrections for multiple comparisons with EEGLAB’s “statcond” and “fdr” functions. We also determined meaningful spectral-power increases or decreases of the theta-band by determining when the power confidence interval was greater or less than zero. We excluded other frequency bands because preliminary analyses showed the main spectral fluctuations were limited to theta. The significance level for all statistical tests was 0.05.

#### *Tests for hypothesis 3: effect of perturbation timing*

We included all perturbed strides to quantify possible motor and electrocortical differences between perturbation timings, i.e., mid-extension and extension onset. For each motor error, we used rANOVA with two factors: 1) *perturbation timing* with two levels: mid-extension and extension-onset, and 2) *task side* also with two levels: left and right. We only performed a post-hoc Student paired t-test between the same side tasks if there was a significant perturbation timing effect. We compared the ERSPs centered around the perturbation event for left-side tasks (i.e., left mid-extension and left extension-onset) and right-side tasks separately. Similar to the tests for hypotheses 1 and 2, we used bootstrapped paired t-tests with corrections for multiple comparisons to compare the theta-band average ERSP between the tasks and determined meaningful spectral-power increases or decreases when the power confidence interval cleared zero. All statistical tests had 0.05 significance level.

#### *Tests for hypothesis 4, motor cortex lateralization*

We compared spectral fluctuations of the cortical clusters during the left and right-side tasks to investigate contralateral and specialized lateralization of the motor cortex. Hemispheric activity that

corresponds to contralateral limb movements is contralateral lateralization whereas hemispheric activity that corresponds with ipsilateral limb movements is specialized lateralization [39]. All perturbed and catch strides were included in this analysis.

## Results

### *Motor error responses and cortical clusters*

Temporal (pacing) and spatial (stepping) errors did not decrease with more exposure to perturbations, and spatial errors did not wash-out (Figure 4.4). Perturbed-stride temporal errors were ~50 ms but catch-stride temporal errors were ~200 ms (Figure 4.3a). The rANOVAs indicated significant temporal error differences in each task ( $F's_{(6,96)} > 40$ ,  $p's < 0.0005$ ). Post-hoc LSD showed a slight temporal error increase during left and right extension-onset perturbed strides and a temporal error decrease during right extension-onset strides post-perturbation. Spatial errors of perturbed strides were steady, ~12° for mid-extension and ~16° for the extension-onset (Figure 4.3b). During the mid-extension tasks, catch-stride spatial errors seemed a continuation of pre-perturbation errors at ~5° but trended to ~10° by the end of the catch strides. rANOVAs were significant for the spatial errors across all tasks ( $F's_{(6,96)} > 29$ ,  $p's < 0.0005$ ). Spatial errors did not wash-out (i.e., return to pre) during post-perturbation (post-hoc LSD  $p's < 0.05$ ). However, post-perturbation spatial errors in the right-side tasks decreased from the first to last batch (LSD  $p's < 0.05$ ).

The optimal k-means identified five cortical clusters (Figure 4.5). We focused on three clusters located at the anterior cingulate cortex (14 subjects), left SMA (13 subjects), and right SMA (13 subjects). Cluster locations were assigned to the nearest Brodmann areas based on the Talairach coordinates of the cluster centroid [34]. As the SMA and premotor cortex share Brodmann area 6, we further confirmed the SMA cluster locations from a previous fMRI and PET meta-analysis [40].

The left and right SMA were determined based on the cluster's centroid location and the individual source locations.

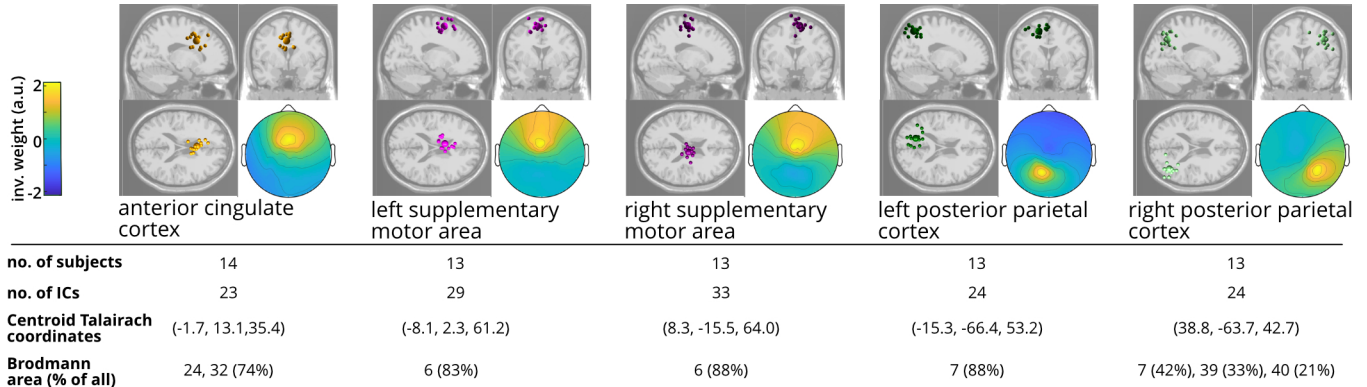


**Figure 4.5: Locations of the electrocortical clusters.** Clusters with sources from > 70% of the subjects are shown. Only one source per subject was selected for each cluster during analysis. "% of all" indicates the percentage of all components in the Brodmann Area. a.u.: arbitrary unit

*Anterior cingulate theta-band adaptation occurred without motor error adaptation in perturbed strides*

Motor errors of the perturbed strides did not decrease from early to late, but anterior cingulate theta-band spectral power decreased in the right-side tasks (Figure 4.6a-c). Neither adaptation nor task side had a significant effect on the perturbed strides (rANOVA, temporal adaptation:  $F_{(1,16)}=0.74$ ,  $p=0.789$ , temporal side:  $F_{(1,16)}=0.74$ ,  $p=0.789$ , spatial adaptation:  $F_{(1,16)}=2.98$ ,  $p=0.104$ , spatial side:  $F_{(1,16)}=0.71$ ,  $p=0.413$ ). Mid-extension perturbed strides had significantly greater average temporal errors (71 vs 39 ms) but smaller spatial errors ( $12^\circ$  vs  $16^\circ$ ) than the extension-onset perturbed strides (rANOVA, temporal:  $F_{(1,16)}=461$ ,  $p<0.0005$ , spatial:  $F_{(1,16)}=30.6$ ,  $p<0.0005$ ). Perturbations elicited anterior cingulate theta synchronization during all tasks (Figure 4.6b). Theta spectral power decreased from early to late for right-side perturbed strides. The left-side perturbed strides, however, had similar and sometimes stronger theta synchronization during late strides than

the early strides. The anterior cingulate cortex also showed theta desynchronization in the recovery steps (i.e., the unperturbed steps after perturbed steps), specifically for the early right-side and late left-side perturbations. The theta-band average ERSP bootstrap t-tests revealed that spectral power had a decreasing trend from early to late for the right-side tasks, which was significant for right mid-extension perturbations (Figure 4.6c). In the left-side perturbed strides, late synchronizations during the recovery steps were statistically different from the non-significant spectral fluctuations during early recovery steps.

*Anterior cingulate theta-band adaptation occurred without motor error adaptation in catch strides*

Motor errors did not increase from early to late catch strides, but early catch strides still elicited theta synchronization in the anterior cingulate cortex (Figure 4.6d-f). Similar to the perturbed strides, neither adaptation nor task side had a significant effect on the temporal or spatial motor errors (rANOVA, temporal-adaptation:  $F_{(1,16)}=3.76$ ,  $p=0.070$ , temporal-side:  $F_{(1,16)}=1.65$ ,  $p=0.217$ , spatial-adaptation:  $F_{(1,16)}=1.43$ ,  $p=0.25$ , spatial-side:  $F_{(1,16)}=0.70$ ,  $p=0.415$ ). Mid-extension catch strides had significantly greater average temporal (250 vs 153 ms) and spatial errors ( $8^\circ$  vs  $6^\circ$ ) than the extension-onset catch strides (rANOVA, temporal:  $F_{(1,16)}=31.9$ ,  $p<0.0005$ , spatial:  $F_{(1,16)}=24.4$ ,  $p<0.0005$ ). Early catch steps elicited anterior cingulate theta synchronization (Figure 4.6e). This synchronization occurred before completion of the catch-step extension for the mid-extension tasks but was near the start of the catch step for just the right extension-onset catch strides. The left mid-extension and right extension-onset elicited theta desynchronization in the recovery steps (Figure 4.6e-f). For right extension-onset, the recovery steps of the late catch strides elicited significantly greater spectral power than the early catch strides.

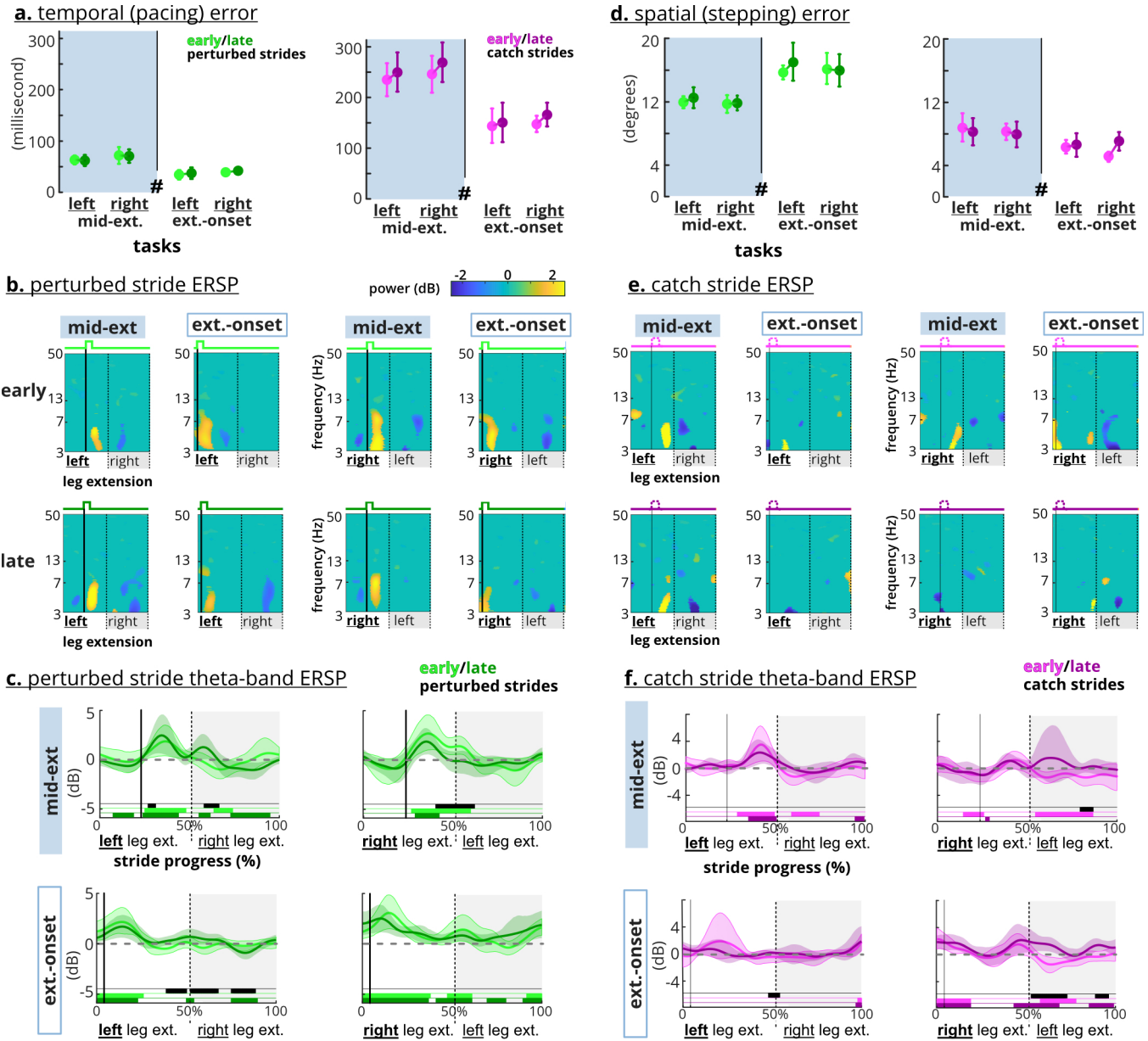


**Figure 4.6: Motor errors and anterior cingulate ERSP**

**a.** and **d.** Adaptation (early vs. late) was not a significant factor for motor errors. # indicates perturbation timing was a significant factor. Error bars indicate confidence interval (CI)

**b.** Perturbations (i.e., the strong solid lines) elicited theta synchronization in anterior cingulate cortex. Right-side perturbations elicited weaker synchronization during the late perturbed strides.

**c.** Average theta-band ERSP waveform shows increased power after the perturbations across the tasks. Late perturbations elicited less theta-band average power only on the right-side tasks.

**e.** Early catches (narrow solid lines) elicited a theta synchronization in the anterior cingulate cortex.

**f.** Average theta-band ERSP waveform shows late right extension-onset catch strides elicited significantly higher spectral power than the early catch. Shaded areas indicate CI. Black bars indicate significant difference between early and late. Colored bars indicate CI does not overlap with zero.

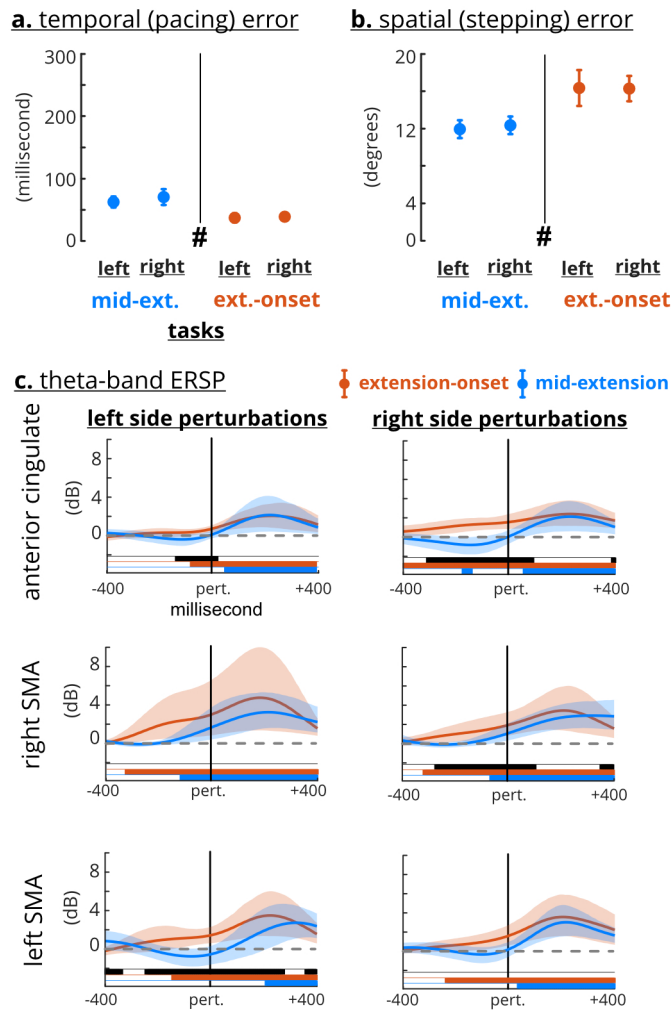


**Figure 4.7: Motor errors and theta-band ERSP across perturbation timings. a. and b.** Task type (mid-extension vs. extension-onset) was a significant factor for motor errors. Error bars indicate confidence interval (CI). **c.** Extension-onset perturbations had greater anterior cingulate and ipsilateral theta-band ERSP before the perturbation event (the solid vertical line). The theta-band ERSP was not significantly different after the perturbation event, except for the left SMA ipsilateral task. Shaded area indicates confidence interval. Black bars indicate significant difference between perturbation timing. Colored bars indicate CI clearing zero.

*Perturbations at extension-onset had greater theta-band ERSP in motor cortices than at mid-extension*

Group analyses including all perturbed strides revealed differential motor error and cortical responses based on perturbation timing (Figure 4.7). Comparing motor errors across all perturbed strides revealed that perturbation timing, and not the task side, was a significant factor (rANOVA, temporal timing:  $F_{(1,16)}=30.5$ ,  $p<0.0005$ , temporal side:  $F_{(1,16)}=2.24$ ,  $p=0.15$ , spatial timing:  $F_{(1,16)}=27.5$ ,  $p<0.0005$ , spatial side:  $F_{(1,16)}=0.25$ ,  $p=0.62$ ) (Figure 4.7a-b). For each side, temporal error was significantly greater during mid-extension than extension-onset and the spatial error was smaller during mid-extension than extension onset (post-hoc paired t-test, temporal right:  $p<0.0005$ , temporal left:  $p=0.001$ , spatial right:  $p<0.0005$ , spatial left:  $p=0.001$ ). The extension-onset perturbations elicited a significant increase in theta-band ERSP before the perturbation event across the anterior cingulate and ipsilateral SMA (Figure 4.7c). The increased theta-band ERSP for mid-extension perturbations was delayed, occurring after the perturbation event in the anterior cingulate and left SMA but was about -100 ms before the perturbation event in the right SMA. Only the ipsilateral left SMA showed greater extension-onset theta-band ERSP than mid-extension for more than 100 ms after the perturbation onset.

*Cortical lateralization and specialization*

The left and right SMAs demonstrated both contralateral and task-specific lateralization with respect to lower limb extension (Figure 4.8). The recovery-step desynchronization during the perturbed strides was most prominent in the right SMA for extension-onset tasks and in the left SMA for the mid-extension tasks, indicating presence of task-specific lateralization (Figure 4.8a, red rectangles). Mid-extension tasks also involved theta desynchronization before the perturbation event in both left and right SMAs (Figure 4.8a, red dashed rectangles). Similar recovery-step desynchronization was

present in the catch strides but were limited to the ipsilateral SMA of the recovery-step leg during extension-onset tasks and to the right SMA for mid-extension tasks (Figure 4.8b, black and red rectangles). Strong theta synchronization only occurred in the right SMA for mid-extension catch strides just before the end of the catch step (Figure 4.8b, red dashed rectangles).

## Discussion

We quantified motor and electrocortical responses to frequent mechanical perturbations during recumbent stepping to gain insight on the electrocortical dynamics of locomotor adaptation. We did not observe typical motor error adaptation. Temporal errors were consistently ~50ms of the desired pace during perturbed strides and returned to pre-perturbation levels in the post block. Spatial errors did not adapt (decrease) with more exposure to the perturbations and did not return to pre-perturbation levels in the post block. The lack of error-based adaptation behavior coupled with small temporal errors and sustained spatial errors in the post block are indicative of use-dependent learning [41]. Electrocortical sources in the anterior cingulate cortex and supplementary motor areas showed that perturbations elicited theta synchronization, as expected. Despite the lack of motor error adaptation, anterior cingulate theta synchronization showed a decreasing trend during late perturbed strides in the right-side tasks. Interestingly, theta-band ERSP during extension-onset tasks started before the perturbation event, resulting in greater theta synchronization in the anterior cingulate and SMAs preceding the perturbation event compared to mid-extension tasks. Motor cortex lateralization was mostly task-specific, where theta desynchronization occurred during the recovery-step in the right SMA for extension-onset tasks but in the left SMA for the mid-extension tasks. These results highlight that electrocortical and motor responses are not necessarily coupled and that perturbation features such as timing could be tuned to elicit greater involvement of specific brain areas.

The perturbed recumbent stepping protocol did not produce the typical error reduction and rapid wash-out associated with motor adaptation, but instead, revealed sustained errors during the post-perturbation block (Figure 4.4), suggesting use-dependent learning occurred. In preliminary analyses, we compared multiple definitions of early and late to determine the robustness of the lack of error-based adaptation in our study. Statistical tests consistently showed no significant difference between early and late, except when early was defined as just the first stride. When perturbations do not directly hinder achieving the task goal, use-dependent learning emerges more than error-based adaptation [41]. With use-dependent learning, motor behaviors are modified in the direction of perturbation and sustained longer after removing the perturbations. Here, we did not provide subjects with any visual feedback of their errors or task performance, so, matching the stepping pace with the pacing cues was the more explicit task goal. Because subjects matched the pacing cues well with temporal errors of ~50 ms, which might be imperceptible for active control adjustments [42], the perturbations did not hinder achieving the task goal. For the less explicit goal of stepping smoothly, however, spatial errors were sustained during perturbed strides and did not wash out during the 2-minute post-perturbation block. During split-crank cycling and split-belt walking where changing muscle recruitment was not an explicit task goal, modified muscular activation patterns were sustained [4, 5]. More recently, a perturbed walking study using brief treadmill belt accelerations during push-off also reported use-dependent learning and sustained post-perturbation gait modifications [43]. Longer-lasting locomotor modifications are desirable for gait rehabilitation and warrant further development of use-dependent learning paradigms.

Perturbations during our seated locomotor task elicited significant anterior cingulate theta synchronization that also decreased with time (i.e. adapted) for right-side perturbations, providing new insights about the anterior cingulate role in error monitoring and motor learning. Previous studies have attributed anterior theta synchronization, or the analogous negative deflection in event-related potentials, to physical loss of balance or presence of a postural threat [15, 44]. Our results

demonstrated that even without a potential loss of balance, mechanical perturbations during a seated locomotor task can elicit anterior cingulate activity. We also observed a trend of adaptation of anterior cingulate theta synchronization for the right-side tasks, which contrasts previous studies that did not observe changes in the anterior cingulate cortex with adaptation but acknowledged a lack of spatial resolution [13, 20]. Our approach likely had sufficient resolution [34, 45], but we observed a trend of anterior cingulate adaptation only in the right-side tasks. Despite consistent motor errors during catch strides, only early catch strides elicited theta synchronization, suggesting that the anterior cingulate perceived early catches as errors, which emphasizes that mechanical perturbations are crucial for anterior cingulate elicitation. Overall, the sustained anterior cingulate theta power across all tasks during perturbed stepping further supports that the anterior cingulate cortex has a role in error-monitoring. However, the theta-band adaptation trend during right-side perturbed stepping suggests that the anterior cingulate also has a role in locomotor learning.

Perturbation timing significantly influenced anterior cingulate theta-band power fluctuations (Figure 4.6), suggesting that tuning perturbation features can modify and stimulate anterior cingulate activity. The theta-band average ERSP for extension-onset perturbations was greater than mid-extension perturbations. This difference may result from an additional intrinsic anterior cingulate theta synchronization that occurs during limb transitions in unperturbed gait, pedaling, and stepping [6, 7, 9, 10]. However, our results did not show significant anterior cingulate activity during pre and post-perturbations strides, partly because our analyses and ICA focused on identifying sources involved in perturbed stepping. The sustained anterior cingulate theta-band elicitation over the entire six minutes of left mid-extension perturbations demonstrates that specific perturbations could be tuned to enhance or extend cortical engagement.

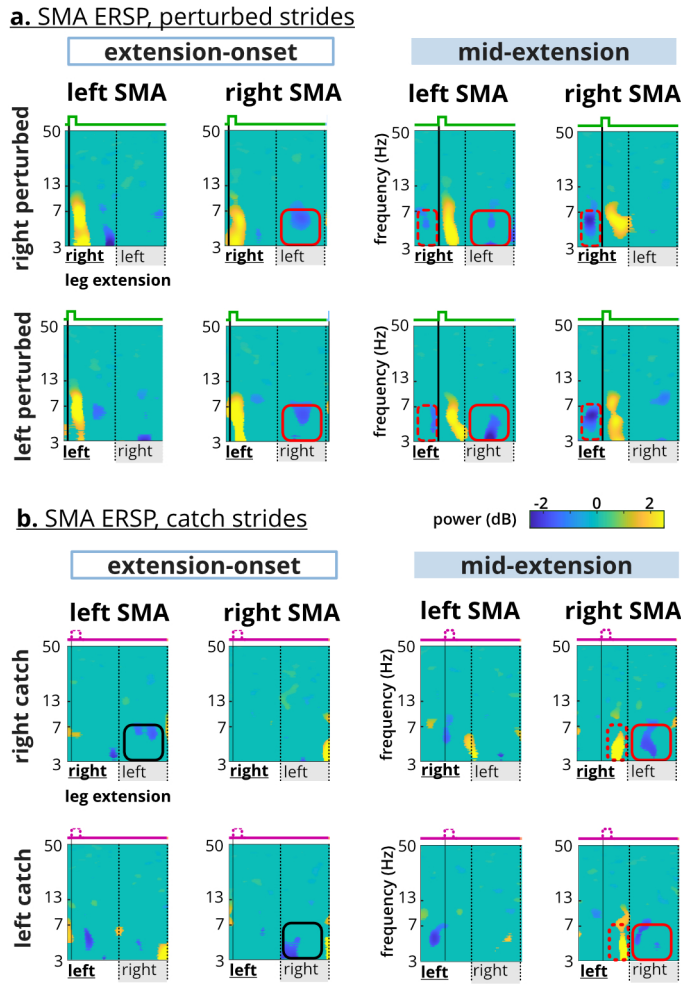


**Figure 4.8: Supplementary motor area (SMA) Lateralization.** **a.** Theta desynchronization in the perturbed recovery step occurred in the right SMA for extension-onset and in the left SMA for the mid-extension (red squares). Only mid-extension perturbations elicited theta desynchronization before the perturbation event (red dashed rectangles). **b.** Mid-extension catch steps elicited theta synchronization before the end of limb extension (red dashed rectangles). Recovery-step theta desynchronization occurred contralaterally during extension-onset, but only occurred in the right SMA during the mid-extension. Red and black indicate specialized and contralateral lateralization respectively.

We identified two close but distinct SMA clusters that exhibited specialized lateralization with both theta synchronization and desynchronization. We were able to identify distinct clusters in close proximity using our novel EEG noise rejection process that performs algorithmic parameter

sweeping to estimate the most brain sources and an optimal k-means clustering algorithm to identify optimal cortical clusters (Figure 4.3). The left and right SMAs had clear differences in theta fluctuations (Figure 4.8), supporting that these SMA clusters were distinct and had specialized responses to the perturbations or motor errors. Theta synchronization occurred exclusively in the right SMA during mid-extension catch steps that had the largest temporal errors (~250 ms), suggesting that despite the lack of a physical perturbation, the right motor area theta synchronization was still sensitive to a motor error. The right motor and premotor cortices have been linked with monitoring temporal aspects of motor tasks [38, 39].

Interestingly, theta desynchronization occurred during the recovery step (i.e., the step following a perturbed step) in the right SMA during extension-onset perturbations and in the left SMA during mid-extension perturbations (Figure 4.8). Previous unperturbed gait studies showed significant theta desynchronization in sensorimotor cortices during mid-stance, but the significance of theta desynchronization specifically is not discussed [6, 7, 9, 10]. A recent study demonstrated that theta synchronization and desynchronization corresponds to negative and positive deflections in event-related potentials (ERP) of motor cortex, respectively [46]. As such, ERP studies provide additional possible interpretations for observed theta synchronization and desynchronization in locomotor tasks. For example, a recent study on upper-limb visuomotor perturbations suggested that the presence (or absence) of negative and positive potentials during perturbations indicated different motor learning strategies [47], which aligns with our results.

Limitations of this study include attributing cortical and motor responses to lower-limb extension and focusing on EEG group-level analyses. We attributed the perturbations to the action of extending the lower-limb, i.e., left mid-extension perturbation means the perturbation occurred in the middle of extending the left-leg. Our stepping torque analysis (not reported here) and a previous study showed that during arms and legs recumbent stepping, subjects mainly relied on lower-limb extension for higher power demands [48]. Ensemble averaging across strides and subjects is necessary for EEG

group-level analysis to reveal event-locked cortical fluctuations [35, 36]. Previous studies had >60 strides per subject for ensemble averaging, inherently increasing their statistical power [15, 38]. We had ~10 catch strides and ~50 perturbed strides per subject and yet were still able to observe distinct event-locked spectral fluctuations. Further single trial analysis may provide more insights into the inter-stride cortical variability [20, 49].

Mechanical perturbations are a robust way to elicit error-related cortical fluctuations and could be tuned to further enhance desired cortical activity. During a seated locomotor task, mechanical perturbations elicited anterior cingulate cortex activity, which decreased with more experience with the right-side perturbations. This supports that the anterior cingulate both monitors errors and learns from them [50]. The left and right SMA clusters demonstrated task-specific lateralization, suggesting that tuning perturbation features such as timing can elicit more desired cortical activity. The uncoupled anterior cingulate activity with motor errors and the specialized SMA fluctuations implicate that cortical feedback may be crucial for closed-loop rehabilitation because motor changes may not adequately reflect cortical dynamics.

## References

- [1] G. Torres-Oviedo, E. Vasudevan, L. Malone, and A. J. Bastian, “Locomotor adaptation,” *Prog. Brain Res.*, vol. 191, pp. 65–74, 2011.
- [2] K. A. Leech, R. T. Roemmich, and A. J. Bastian, “Creating flexible motor memories in human walking,” *Sci. Rep.*, vol. 8, p. 94, Jan. 2018.
- [3] J. T. Choi and A. J. Bastian, “Adaptation reveals independent control networks for human walking,” *Nat. Neurosci.*, vol. 10, pp. 1055–1062, Aug. 2007.

- [4] L. Alibiglou and D. A. Brown, “Relative temporal leading or following position of the contralateral limb generates different aftereffects in muscle phasing following adaptation training post-stroke,” *Exp. Brain Res.*, vol. 211, pp. 37–50, May 2011.
- [5] M. J. MacLellan, Y. P. Ivanenko, F. Massaad, S. M. Bruijn, J. Duysens, and F. Lacquaniti, “Muscle activation patterns are bilaterally linked during split-belt treadmill walking in humans,” *J. Neurophysiol.*, vol. 111, pp. 1541–1552, Apr. 2014.
- [6] K. Gramann, J. T. Gwin, D. P. Ferris, K. Oie, T.-P. Jung, C.-T. Lin, L.-D. Liao, and S. Makeig, “Cognition in action: imaging brain/body dynamics in mobile humans,” *Rev. Neurosci.*, vol. 22, pp. 593–608, Nov. 2011.
- [7] H. Enders, F. Cortese, C. Maurer, J. Baltich, A. B. Protzner, and B. M. Nigg, “Changes in cortical activity measured with EEG during a high-intensity cycling exercise,” *J. Neurophysiol.*, vol. 115, pp. 379–388, Jan. 2016.
- [8] D. C. Hinton, A. Thiel, J.-P. Soucy, L. Bouyer, and C. Paquette, “Adjusting gait step-by-step: Brain activation during split-belt treadmill walking,” *Neuroimage*, vol. 202, p. 116095, Nov. 2019.
- [9] T. C. Bulea, J. Kim, D. L. Damiano, C. J. Stanley, and H.-S. Park, “Prefrontal, posterior parietal and sensorimotor network activity underlying speed control during walking,” *Front. Hum. Neurosci.*, vol. 9, p. 247, May 2015.
- [10] J. E. Kline, H. J. Huang, K. L. Snyder, and D. P. Ferris, “Cortical spectral activity and connectivity during active and viewed arm and leg movement,” *Front. Neurosci.*, vol. 10, p. 91, Mar. 2016.

- [11] L. Jaeger, L. Marchal-Crespo, P. Wolf, R. Riener, L. Michels, and S. Kollias, “Brain activation associated with active and passive lower limb stepping,” *Front. Hum. Neurosci.*, vol. 8, p. 828, Oct. 2014.
- [12] A. D. Nordin, W. D. Hairston, and D. P. Ferris, “Faster gait speeds reduce alpha and beta EEG spectral power from human sensorimotor cortex,” *IEEE Trans. Biomed. Eng.*, June 2019.
- [13] J. Haefeli, S. Vögeli, J. Michel, and V. Dietz, “Preparation and performance of obstacle steps: interaction between brain and spinal neuronal activity,” *Eur. J. Neurosci.*, vol. 33, pp. 338–348, Jan. 2011.
- [14] L. Marchal-Crespo, L. Michels, L. Jaeger, J. López-Olóriz, and R. Riener, “Effect of error augmentation on brain activation and motor learning of a complex locomotor task,” *Front. Neurosci.*, vol. 11, p. 526, Sept. 2017.
- [15] S. M. Peterson and D. P. Ferris, “Differentiation in theta and beta electrocortical activity between visual and physical perturbations to walking and standing balance,” *eNeuro*, vol. 5, July 2018.
- [16] A. D. Nordin, W. D. Hairston, and D. P. Ferris, “Human electrocortical dynamics while stepping over obstacles,” *Sci. Rep.*, vol. 9, p. 4693, Mar. 2019.
- [17] K. R. Ridderinkhof, M. Ullsperger, E. A. Crone, and S. Nieuwenhuis, “The role of the medial frontal cortex in cognitive control,” *Science*, vol. 306, pp. 443–447, Oct. 2004.
- [18] J. M. Galea, A. Vazquez, N. Pasricha, J.-J. O. de Xivry, and P. Celnik, “Dissociating the roles of the cerebellum and motor cortex during adaptive learning: the motor cortex retains what the cerebellum learns,” *Cereb Cortex*, vol. 21, pp. 1761–1770, Aug. 2011.
- [19] P. Arrighi, L. Bonfiglio, F. Minichilli, N. Cantore, M. C. Carboncini, E. Piccotti, B. Rossi, and P. Andre, “EEG theta dynamics within frontal and parietal cortices for error processing during

reaching movements in a prism adaptation study altering visuo-motor predictive planning,” *PLoS One*, vol. 11, no. 3, p. e0150265, 2016.

- [20] A. Mierau, T. Hülsdünker, and H. K. Strüder, “Changes in cortical activity associated with adaptive behavior during repeated balance perturbation of unpredictable timing,” *Front. Behav. Neurosci.*, vol. 9, p. 272, Oct. 2015.
- [21] A. M. Payne and L. H. Ting, “Worse balance is associated with larger perturbation-evoked cortical responses in healthy young adults,” *Gait Posture*, vol. 80, pp. 324–330, June 2020.
- [22] R. H. Stoloff, E. P. Zehr, and D. P. Ferris, “Recumbent stepping has similar but simpler neural control compared to walking,” *Exp. Brain Res.*, vol. 178, pp. 427–438, Apr. 2007.
- [23] E. P. Zehr, J. E. Balter, D. P. Ferris, S. R. Hundza, P. M. Loadman, and R. H. Stoloff, “Neural regulation of rhythmic arm and leg movement is conserved across human locomotor tasks,” *J. Physiol.*, vol. 582, pp. 209–227, July 2007.
- [24] H. J. Huang and D. P. Ferris, “Upper and lower limb muscle activation is bidirectionally and ipsilaterally coupled,” *Med. Sci. Sports Exerc.*, vol. 41, pp. 1778–1789, Sept. 2009.
- [25] E.-R. Symeonidou, A. D. Nordin, W. D. Hairston, and D. P. Ferris, “Effects of cable sway, electrode surface area, and electrode mass on electroencephalography signal quality during motion,” *Sensors*, vol. 18, Apr. 2018.
- [26] A. Delorme and S. Makeig, “EEGLAB: an open source toolbox for analysis of single-trial EEG dynamics including independent component analysis,” *J. Neurosci. Methods*, vol. 134, pp. 9–21, Mar. 2004.
- [27] T. Mullen, “CleanLine: Tool/Resource info.” <https://www.nitrc.org/projects/cleanline/>, Feb. 2012. Accessed: 2019-5-10.

- [28] I. Winkler, S. Debener, K.-R. Müller, and M. Tangermann, “On the influence of high-pass filtering on ICA-based artifact reduction in EEG-ERP,” in *37th Annual International Conference of the IEEE Engineering in Medicine and Biology Society (EMBC)*, Aug. 2015.
- [29] A. S. Oliveira, B. R. Schlink, W. D. Hairston, P. König, and D. P. Ferris, “A channel rejection method for attenuating Motion-Related artifacts in EEG recordings during walking,” *Front. Neurosci.*, vol. 11, p. 225, Apr. 2017.
- [30] J. A. Palmer, S. Makeig, K. Kreutz-Delgado, and B. D. Rao, “Newton method for the ICA mixture model,” in *2008 IEEE International Conference on Acoustics, Speech and Signal Processing*, pp. 1805–1808, Mar. 2008.
- [31] L. Pion-Tonachini, S. Makeig, and K. Kreutz-Delgado, “Crowd labeling latent dirichlet allocation,” *Knowl. Inf. Syst.*, vol. 53, pp. 749–765, Dec. 2017.
- [32] B. Hjorth, “An on-line transformation of EEG scalp potentials into orthogonal source derivations,” *Electroencephalogr. Clin. Neurophysiol.*, vol. 39, pp. 526–530, Nov. 1975.
- [33] J. L. Lancaster, M. G. Woldorff, L. M. Parsons, M. Liotti, C. S. Freitas, L. Rainey, P. V. Kochunov, D. Nickerson, S. A. Mikiten, and P. T. Fox, “Automated talairach atlas labels for functional brain mapping,” *Hum. Brain Mapp.*, vol. 10, pp. 120–131, July 2000.
- [34] S. Y. Shirazi and H. J. Huang, “More reliable EEG electrode digitizing methods can reduce source estimation uncertainty, but current methods already accurately identify brodmann areas,” *Front. Neurosci.*, vol. 13, p. 1159, 2019.
- [35] S. Makeig, “Auditory event-related dynamics of the EEG spectrum and effects of exposure to tones,” *Electroencephalogr. Clin. Neurophysiol.*, vol. 86, pp. 283–293, Apr. 1993.
- [36] G. Pfurtscheller and F. H. Lopes da Silva, “Event-related EEG/MEG synchronization and desynchronization: basic principles,” *Clin. Neurophysiol.*, vol. 110, pp. 1842–1857, Nov. 1999.

- [37] J. van Leeuwen, J. B. J. Smeets, and A. V. Belopolsky, “Forget binning and get SMART: Getting more out of the time-course of response data,” *Atten. Percept. Psychophys.*, vol. 81, pp. 2956–2967, Nov. 2019.
- [38] J. Wagner, S. Makeig, M. Gola, C. Neuper, and G. Müller-Putz, “Distinct  $\beta$  band oscillatory networks subserving motor and cognitive control during gait adaptation,” *J. Neurosci.*, vol. 36, pp. 2212–2226, Feb. 2016.
- [39] P. K. Mutha, L. H. Stapp, R. L. Sainburg, and K. Y. Haaland, “Frontal and parietal cortex contributions to action modification,” *Cortex*, vol. 57, pp. 38–50, Aug. 2014.
- [40] M. A. Mayka, D. M. Corcos, S. E. Leurgans, and D. E. Vaillancourt, “Three-dimensional locations and boundaries of motor and premotor cortices as defined by functional brain imaging: a meta-analysis,” *Neuroimage*, vol. 31, pp. 1453–1474, July 2006.
- [41] J. Diedrichsen, O. White, D. Newman, and N. Lally, “Use-dependent and error-based learning of motor behaviors,” *J. Neurosci.*, vol. 30, pp. 5159–5166, Apr. 2010.
- [42] M. G. Carpenter, J. H. J. Allum, and F. Honegger, “Directional sensitivity of stretch reflexes and balance corrections for normal subjects in the roll and pitch planes,” *Exp. Brain Res.*, vol. 129, pp. 93–113, Oct. 1999.
- [43] A. Farrens, M. Lilley, and F. Sergi, “Training propulsion via acceleration of the trailing limb,” *IEEE Trans. Neural Syst. Rehabil. Eng.*, pp. 1–1, 2020.
- [44] A. L. Adkin, A. D. Campbell, R. Chua, and M. G. Carpenter, “The influence of postural threat on the cortical response to unpredictable and predictable postural perturbations,” *Neurosci. Lett.*, vol. 435, pp. 120–125, Apr. 2008.

- [45] S. Y. Shirazi and H. J. Huang, “Influence of mismarking fiducial locations on EEG source estimation\*,” in *2019 9th International IEEE/EMBS Conference on Neural Engineering (NER)*, pp. 377–380, Mar. 2019.
- [46] S. Nakagome, T. P. Luu, Y. He, A. S. Ravindran, and J. L. Contreras-Vidal, “An empirical comparison of neural networks and machine learning algorithms for EEG gait decoding,” *Sci. Rep.*, vol. 10, p. 4372, Mar. 2020.
- [47] D. J. Palidis, J. G. A. Cashaback, and P. L. Gribble, “Neural signatures of reward and sensory error feedback processing in motor learning,” *J. Neurophysiol.*, vol. 121, pp. 1561–1574, Apr. 2019.
- [48] N. E. Skinner, *Subjective Costs of Movement: Factors beyond Economy in Human Behavior*. PhD thesis, University of Michigan, 2014.
- [49] J. Wagner, R. Martínez-Cancino, and S. Makeig, “Trial-by-trial source-resolved EEG responses to gait task challenges predict subsequent step adaptation,” *Neuroimage*, vol. 199, pp. 691–703, Oct. 2019.
- [50] C. B. Holroyd and M. G. H. Coles, “The neural basis of human error processing: reinforcement learning, dopamine, and the error-related negativity,” *Psychol. Rev.*, vol. 109, pp. 679–709, Oct. 2002.

## **APPENDIX A: IRB DOCUMENTS**



UNIVERSITY OF CENTRAL FLORIDA

**Institutional Review Board**  
FWA00000351  
IRB00001138  
Office of Research  
12201 Research Parkway  
Orlando, FL 32826-3246

CLOSURE

December 4, 2020

Dear [Helen Huang](#):

On 12/4/2020, the IRB reviewed the following protocol:

Type of Review:	Continuing Review
Title:	Brain and muscle responses to stepping errors during rhythmic exercise
Investigator:	<a href="#">Helen Huang</a>
IRB ID:	CR00000840
Funding:	Name: National Institute on Aging (NIA), Funding Source ID: R01AG054621
Grant ID:	None
IND, IDE, or HDE:	None

The IRB acknowledges your request for closure of the protocol effective as of 12/4/2020. As part of this action:

- The protocol is permanently closed to enrollment.
- All subjects have completed all protocol-related interventions.
- Collection of private identifiable information is completed.
- Analysis of private identifiable information is completed.

If you have any questions, please contact the UCF IRB at 407-823-2901 or [irb@ucf.edu](mailto:irb@ucf.edu). Please include your project title and IRB number in all correspondence with this office.

Sincerely,

Racine Jacques, Ph.D.  
Designated Reviewer



UNIVERSITY OF CENTRAL FLORIDA

**Institutional Review Board**

FWA00000351  
IRB00001138Office of Research  
12201 Research Parkway  
Orlando, FL 32826-3246

APPROVAL

November 27, 2019

Dear Helen Huang:

On 11/27/2019, the IRB reviewed the following submission:

Type of Review:	Modification and Continuing Review
Title:	Brain and muscle responses to stepping errors during rhythmic exercise
Investigator:	Helen Huang
IRB ID:	MODCR00000307
Funding:	Name: National Institute on Aging (NIA), Funding Source ID: R01AG054621
Grant ID:	None
IND, IDE, or HDE:	None
Documents Reviewed:	<ul style="list-style-type: none"><li>• r01-rs-ad.docx, Category: Recruitment Materials;</li><li>• r01-rs-bbs.pdf, Category: Test Instruments;</li><li>• r01-rs-champs.pdf, Category: Survey / Questionnaire;</li><li>• r01-rs-consent-c1.pdf, Category: Consent Form;</li><li>• r01-rs-email.docx, Category: Recruitment Materials;</li><li>• r01-rs-flyer.doc, Category: Recruitment Materials;</li><li>• r01-rs-msse.pdf, Category: Test Instruments;</li><li>• r01-rs-phonesurvey.doc, Category: Survey / Questionnaire;</li><li>• r01-rs-protocol-c1.doc, Category: IRB Protocol;</li><li>• r01-rs-sppb.doc, Category: Test Instruments;</li><li>• r01-rs-subjinfo.docx, Category: Survey / Questionnaire;</li></ul>

The IRB approved the protocol from 11/27/2019 to 11/26/2020.

In conducting this protocol, you are required to follow the requirements listed in the Investigator Manual (HRP-103), which can be found by navigating to the IRB Library within the IRB system.

If you have any questions, please contact the UCF IRB at 407-823-2901 or [irb@ucf.edu](mailto:irb@ucf.edu). Please include your project title and IRB number in all correspondence with this office.

Sincerely,

Adrienne Showman  
Designated Reviewer



Approved

Entered IRB: 11/17/2019 5:38 PM  
Approval: 11/27/2019  
Initial effective: 11/27/2019  
Effective: 11/27/2019  
Last updated: 11/27/2019 12:45 PM

## Next Steps

[View Modification/CR](#)[Add Comment](#)

(IRB - MOD/CR - Review Complete)

## MODCR00000307: Modification and Continual Review #1 for Study Brain and muscle response to stepping errors during rhythmic exercise

Principal investigator: Helen Huang

Submission type: Modification and Continuing Review

Primary contact:

IRB office:

UCF IRB

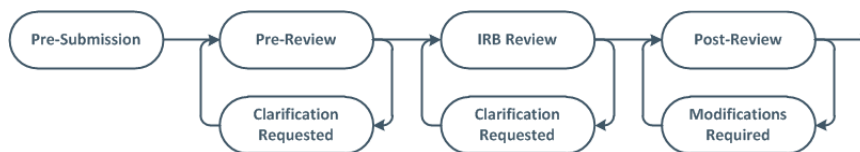
IRB coordinator:

Adrienne Showman

Letter:

Correspondence for...

Regulatory authority: Pre-2018 Requirements

[History](#) [Contacts](#) [CITI Training](#) [Documents](#) [Reviews](#) [Related RNIs](#) [Snapshots](#)**Principal Investigator**

Name	Financial Interest	E-mail
Helen Huang	no	hhuang@ucf.edu

**Study Team**

Name	Roles	Financial Interest	Involved in Consent	E-mail
Cesar Castano	Research Assistant	no	yes	castanocesar
Jinfeng Li	Research Assistant	no	yes	jinfeng@knigh...
Seyed Yahya Shirazi	Research Assistant	no	yes	seyed@knigh...

**Other Study Team Member Information**

Document	Description
----------	-------------

**Guests Who Can View This Submission**

Name	E-mail	Phone
------	--------	-------

## **APPENDIX B: COPYRIGHT PERMISSION LETTERS**

February 24, 2021

12201 Research Pkwy  
Suite 150B  
Orlando, FL 32826

We, Seyed Yahya Shirazi and Helen J. Huang, the copyright holders of the paper entitled *Differential theta-band signatures of the anterior cingulate and motor cortices during seated locomotor perturbations* grant the permission to reprint this paper in Seyed Yahya Shirazi's dissertation entitled *Corticomuscular adaptation to mechanical perturbations in a seated locomotor task*.

This permission extends to any future revisions and editions of Mr. Shirazi's dissertation, including non-exclusive world rights in all languages. These rights will in no way restrict republication of the material in any other form by the copyright holders.

Paper's full citation:

Shirazi, Seyed Yahya, and Helen J. Huang. 2021. "Differential Theta-Band Signatures of the Anterior Cingulate and Motor Cortices during Seated Locomotor Perturbations." IEEE Transactions on Neural Systems and Rehabilitation Engineering: A Publication of the IEEE Engineering in Medicine and Biology Society PP (February). <https://doi.org/10.1109/TNSRE.2021.3057054>.

Seyed Yahya Shirazi

Helen J. Huang

February 24, 2021

12201 Research Pkwy  
Suite 150B  
Orlando, FL 32826

We, Seyed Yahya Shirazi and Helen J. Huang, the copyright holders of the paper entitled *More Reliable EEG Electrode Digitizing Methods Can Reduce Source Estimation Uncertainty, but Current Methods Already Accurately Identify Brodmann Areas* grant the permission to reprint this paper in Seyed Yahya Shirazi's dissertation entitled *Corticolumbar adaptation to mechanical perturbations in a seated locomotor task*.

This permission extends to any future revisions and editions of Mr. Shirazi's dissertation, including non-exclusive world rights in all languages. These rights will in no way restrict republication of the material in any other form by the copyright holders.

Paper's full citation:

Shirazi, Seyed Yahya, and Helen J. Huang. 2019. "More Reliable EEG Electrode Digitizing Methods Can Reduce Source Estimation Uncertainty, but Current Methods Already Accurately Identify Brodmann Areas." *Frontiers in Neuroscience* 13: 1159.

Seyed Yahya Shirazi

Helen J. Huang

February 24, 2021

12201 Research Pkwy  
Suite 150B  
Orlando, FL 32826

We, Seyed Yahya Shirazi and Helen J. Huang, the copyright holders of the paper entitled *Influence of mis-marking fiducial locations on EEG source estimation* grant the permission to reprint this paper in Seyed Yahya Shirazi's dissertation entitled *Corticomuscular adaptation to mechanical perturbations in a seated locomotor task*.

This permission extends to any future revisions and editions of Mr. Shirazi's dissertation, including non-exclusive world rights in all languages. These rights will in no way restrict republication of the material in any other form by the copyright holders.

Paper's full citation:

Shirazi, Seyed Yahya, and Helen J. Huang. 2019. "Differential Theta-Band Signatures of the Anterior Cingulate and Motor Cortices during Seated Locomotor Perturbations." bioRxiv 544288. <https://doi.org/10.1101/544288>.

Seyed Yahya Shirazi

Helen J. Huang